Supplementary Information for

Mechanistic Insights into Hydrophobicity-Dependent Antimicrobial Selectivity of Quaternary Ammonium Poly(oxanorborneneimide) Polymers Using Coarse-Grained Simulations

Joshua D. Richardson,[1] Vincent M. Rotello,[3] and Reid C. Van Lehn[1,2,*]

[1]Department of Chemical and Biological Engineering, University of Wisconsin – Madison, Madison, WI, 53706, USA.
[2]Department of Chemistry, University of Wisconsin – Madison, Madison, WI, 53706, USA.
[3]Department of Chemistry, University of Massachusetts, Amherst, MA, 01003, USA.
*address correspondence to: vanlehn@wisc.edu

To quantitatively compare the hydrophobicity of the four PONI polymer side chains modeled in this study (**Figure 1a**), we utilized the SwissADME tool[1] to calculate n-octanol/water partition coefficient values (log $P_{o/w}$) for each monomer unit. Log $P_{o/w}$ reflects the balance between the lipophilicity and hydrophilicity of a compound, with more positive values indicating increased lipophilicity (hydrophobicity) and more negative values indicating increased hydrophilicity. SwissADME reports an average log $P_{o/w}$ from five predictive models, with values for PONI polymer side chains tabulated in **Table S1**.

Table S1: N-octanol/water partition coefficient (log P*o/w*) values for each PONI polymer side chain (structures in main text **Figure 1a**) calculated with the SwissADME tool.

	Log $P_{o/w}$
P1	-1.88
P3	-0.63
P5	1.22
P9	4.41

To model bacterial (*E. coli*, MRSA) and human red blood cell (RBC) membranes in this study, we utilized a diverse set of lipid parameters available in the MARTINI 3 force field.[2] These include parameters for tetraoleoyl cardiolipin (TOCL), palmitoyl-oleoyl phospholipids (POPG, POPE, POPC, POPS), sphingomyelin (POSM), and cholesterol (CHOL). However, to our knowledge, MARTINI 3 parameters for cationic lysyl-phosphatidylglycerol (lysyl-PG) lipids found in high abundance in Gram-positive bacterial membranes such as MRSA are not currently available. Therefore, we developed a parameterization strategy to incorporate a new lysyl-PG lipid type derived from POPG with an additional L-lysine moiety, which we denote as POPGK (**Figure 1b**).

We first prepared parameters for atomistic POPGK (**Figure S1a**) by combining CHARMM36 lysyl-DPPG (DPPGK) headgroup parameters with POPG glycerol linker and tail parameters available in the CHARMM-GUI server,[3] consistent with previous atomistic MD studies that have constructed lysyl-PG parameters from lipid fragments for use in Gram-positive bacterial membrane models.[4, 5] To parameterize a coarse-grained MARTINI 3 model, we then performed atomistic simulations of 64-lipid POPGK membranes. This involved 5000 steps of energy minimization with steepest descent with a maximum step size of 0.01 nm, followed by four equilibration steps: (1) *NVT* with a 1 fs timestep and heavy atom position restraints, (2) *NPT* with a 1 fs timestep and heavy atom position restraints, (3) *NPT* with a 2 fs timestep and heavy atom position restraints, and (4) *NPT* with a 2 fs timestep. *NPT* equilibration steps utilized semi-isotropic pressure coupling with the Berendsen barostat, 4.5 x 10^{-5} bar^{-1} compressibility, and a 5 ps time constant to control the pressure at 1 bar. All other simulation parameters followed the workflow presented in the '**Atomistic Simulations of PONI Polymers**' section in the main text (e.g., temperature coupling at 310 K, bonded interaction cutoffs). Equilibration was followed by a 50 ns *NPT* production simulation with pressure controlled with the Parrinello-Rahman barostat, and all simulations were repeated for three independent replicas.

To parameterize the new headgroup of POPGK for MARTINI, we mapped atoms to best match constituent POPG glycerol-phosphate (blue ovals in **Figure S1a**) and L-lysine (red ovals) groups. We inherited the following bead types from MARTINI 3 POPG and L-lysine parameters: PO4 = 'Q5', BB = 'Q5', SC1 = 'SC3', SC2 = 'SQ4p'. We decreased the polarity of the glycerol GL0 bead from 'P4r' to 'P1' to account for the esterification with L-lysine. All bonded parameters contained entirely within either the L-lysine or POPG region were adapted directly from MARTINI 3. Bonded parameters between these regions (BB-GL0, SC1-BB-GL0, BB-GL0-PO4) were iteratively parameterized with 64-lipid coarse-grained membrane simulations to match mapped atomistic distributions most closely (**Figure S1b**). These coarse-grained simulations utilized the following workflow: (1) energy minimization with the steepest descent algorithm for 2000 steps with a maximum 0.01 nm step size, (2) 50 ns *NPT* equilibration, and (3) 50 ns *NPT* production. Equilibration and production steps utilized the same simulation parameters as the '**Polymer-Membrane Simulations**' section in the main text, and all simulations were repeated for three independent replicas.

Area per lipid and bilayer thickness metrics were compared between production simulations of atomistic and coarse-grained membranes (**Figure S1c**). The area per lipid was calculated by multiplying the average box lengths in the *x* and *y* dimensions calculated with *gmx energy* and normalizing by the 32 lipids in the upper leaflet. Bilayer thickness was determined from the average density profile of phosphate P atoms (atomistic simulations) or PO4 beads (coarse-grained simulations) using 200 slices in the *z*-direction with *gmx density* by calculating the distance between the two peak maxima. Both metrics are in excellent agreement between atomistic and coarse-grained simulations (within 3% difference, **Figure S1c)**, accurately capturing the decreased packing caused by the bulky lysyl-PG headgroup of POPGK compared to standard palmitoyl-oleoyl phospholipids.[6, 7]

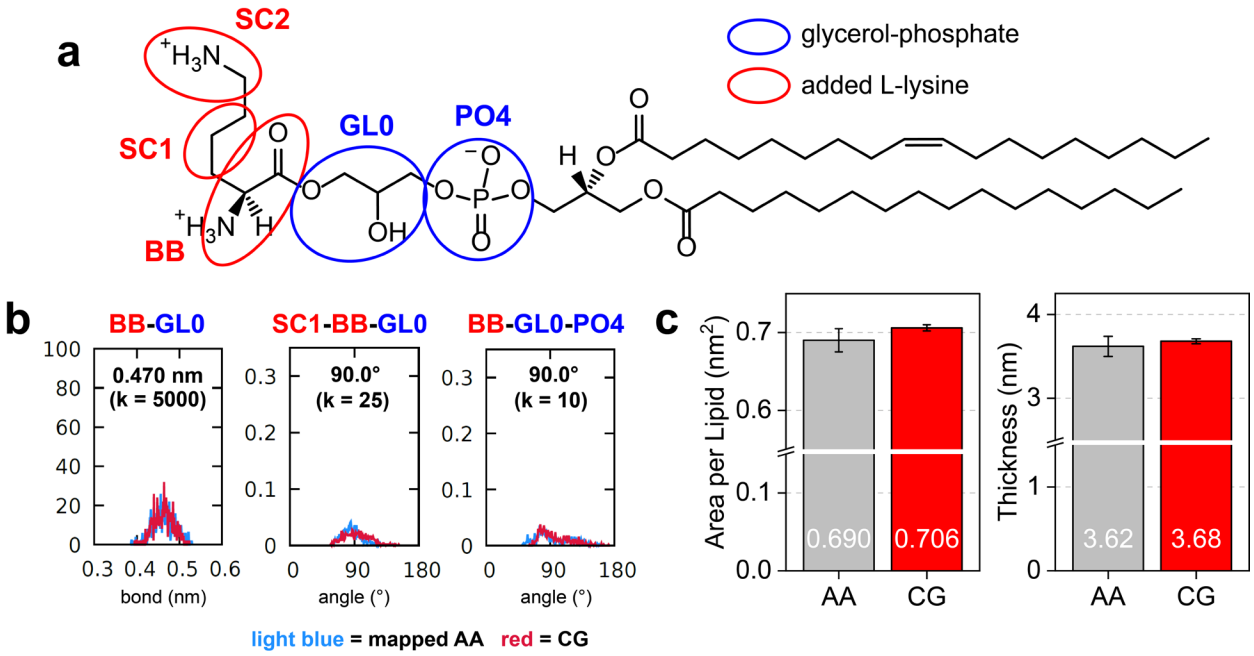

Figure S1: (a) Mapping strategy for the POPGK headgroup, denoting glycerol-phosphate (blue) and L-lysine (red) regions. (b) Newly parameterized bond (BB-GL0) and angles (SC1-BB-GL0, BB-GL0-PO4) for the POPGK headgroup, demonstrating agreement between mapped all-atom (AA) and coarse-grained (CG) simulations with corresponding values and force contants (k) used in CG simulations. (c) Comparison of average area per lipid (left) and thickness (right) metrics between AA (gray) and CG (red) simulations across three independent replicas. Error bars denote standard devations.

Table S2 summarizes the lipid counts in the upper and lower leaflets of the *E. coli*, MRSA, and RBC membrane models used in this study (**Figure 1b**). All membranes were initalized with the *insane* tool[8] as discussed in the '**Polymer and Membrane Selection**' section of the main text. Bacterial membranes (*E. coli*, MRSA) were constructed with symmetric lipid compositions in both leaflets, whereas RBC membranes were constructed with an asymmetric lipid distribution between leaflets and high cholesterol (CHOL) content (~50%) consistent with the MARTINI RBC model utilized in our previous work.[6] Lipids in **Table S2** are color coded as follows: Blue = cationic, red = anionic, black = zwitterionic. Lipid counts were chosen to closely match total membrane areas across bare membrane systems (gray bars in **Figure S2**), which demonstate areas within 3% of one another. Maintaining comparable membrane areas is critical to ensure that observed differences in polymer-membrane interactions across membrane types (e.g., binding, insertion, disruption) arise from differences in lipid composition only and not differences in membrane surface availability.

Table S2: Lipid counts in upper and lower leaflets of *E. coli*, MRSA, and RBC (**Figure 1b**).

		E. coli	MRSA	RBC
Upper Leaflet	POPGK	-	183	-
	TOCL	26	24	-
	POPG	105	275	-
	POPE	396	-	38
	POPC	-	-	174
	POSM	-	-	174
	POPS	-	-	-
	CHOL	-	-	387

Lower Leaflet	POPGK	-	183	-
	TOCL	26	24	-
	POPG	105	275	-
	POPE	396	-	176
	POPC	-	-	78
	POSM	-	-	39
	POPS	-	-	98
	CHOL	-	-	392

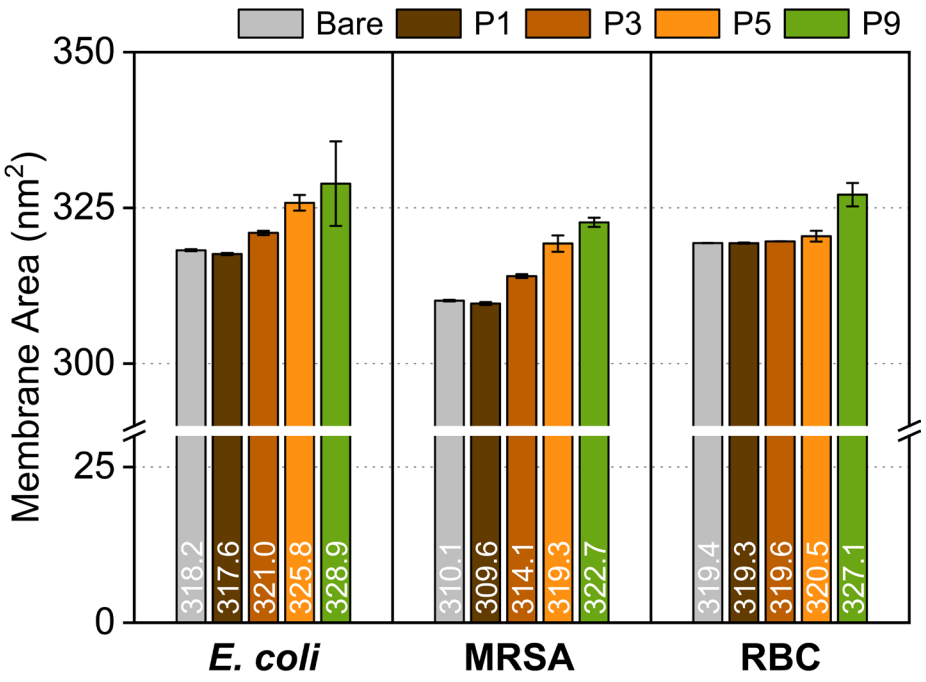

Figure S2: Average membrane areas calculated across three independent replicas for bare membrane systems (gray) and membrane systems containing P1 (dark brown), P3 (light brown), P5 (orange), and P9 (green) polymers. Error bars denote standard deviations.

Figure S3 summarizes the workflow used to initialize atomistic PONI polymers for simulation in water as described in the '**Atomistic Simulations of PONI Polymers**' section in the main text. First, a single monomer template (.pdb) is created using Avogadro[9] and placed in an empty simulation box using the *gmx editconf* command in Gromacs (**Figure S3a**). The -box and -rotate flags of *editconf* are used to align the monomer in the *xy*-plane with appropriate spacing in the *x*-direction for subsequent monomer addition. The *gmx genconf* command is then used to replicate this monomer 64 times in the *x*-direction (-nbox 64 1 1) to create an initial all-*cis* version of a PONI polymer (**Figure S3b**). We then utilize an in-house python script to randomly rotate monomers along the polymer backbone to generate polymers with randomized *cis*/*trans* alkene distributions (**Figure S3c**), targeting a ~50:50 *cis*/*trans* distribution (32 *trans*, 31 *cis*) as shown in **Figure 2a**. In parallel, we conduct a workflow to parameterize terminal (beg, end) and internal (mid) polymer residues for use with the CHARMM36 force field. First, a three-monomer structure is created in Avogadro (**Figure S3d**) and saved as a .mol2 file, which is uploaded to the CGenFF web server[10] to assign atom types, partial charges, and bonded parameters for chemical motifs in PONI polymers not present in standard CHARMM36 polymer libraries.[11] These parameters are converted to .rtp file format (**Figure S3e**) that includes all residues (beg, mid, end), and the *gmx pdb2gmx* command in Gromacs is used to create a topology file for the initial structure (**Figure S3c**).

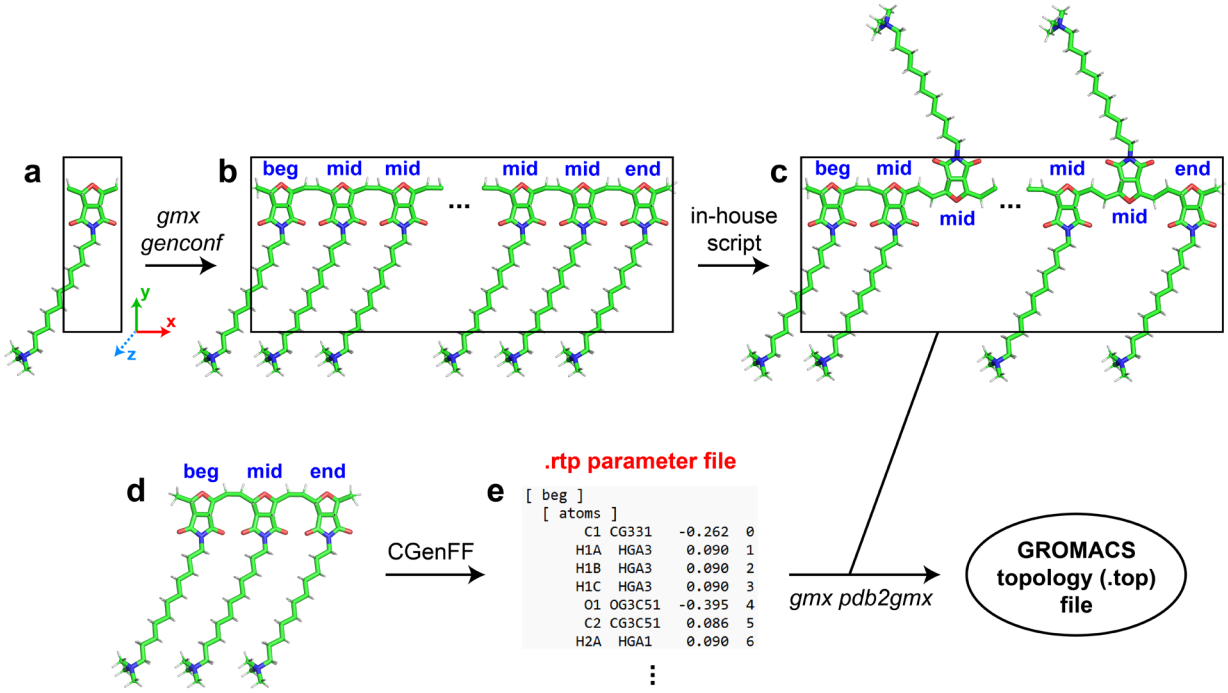

Figure S3: Workflow for creating an initial atomistic PONI polymer structure. (a) A single monomer is placed in an empty simulation box. (b) The monomer is replicated 64 times in the *x*-direction and (c) converted into a randomized 64-mer targeting a ~50:50 *cis*/*trans* alkene distribution. In parallel, (d) a 3-mer structure is uploaded to the CGenFF web server to generate polymer parameters, which are (e) converted to .rtp file format compatible with *gmx pdb2gmx* to generate the polymer topology (.top).

Prior to CG mapping, all atomistic polymer structures were subjected to a 10 ns equilibration (**Figure 2b**) to allow relaxation from an initially fully extended conformation (**Figure 2a**). **Figure S4** demonstrates this process for a P5 polymer. The end-to-end distance (d_{ee}) decreases substantially over the course of the simulation (**Figure S4a**), reflecting collapse of the polymer backbone to a compact equilibrated structure. We also visualize the convergence of a *cis* and *trans* mapped B0-BL-B0 angle during atomistic equilibration, with convergence to their expected equilibrium values of 90° and 175°, respectively (**Figure S4b**), consistent with CG bonded parameters (**Figures S10-S11**). Together, these results demonstrate the importance of the 10 ns atomistic equilibration step (**Figure 2b**) in our workflow to ensure that bonded distributions in the mapped CG structure (**Figure 2c**) are physically reasonable and do not produce forces that destabilize the system at the start of CG simulation.

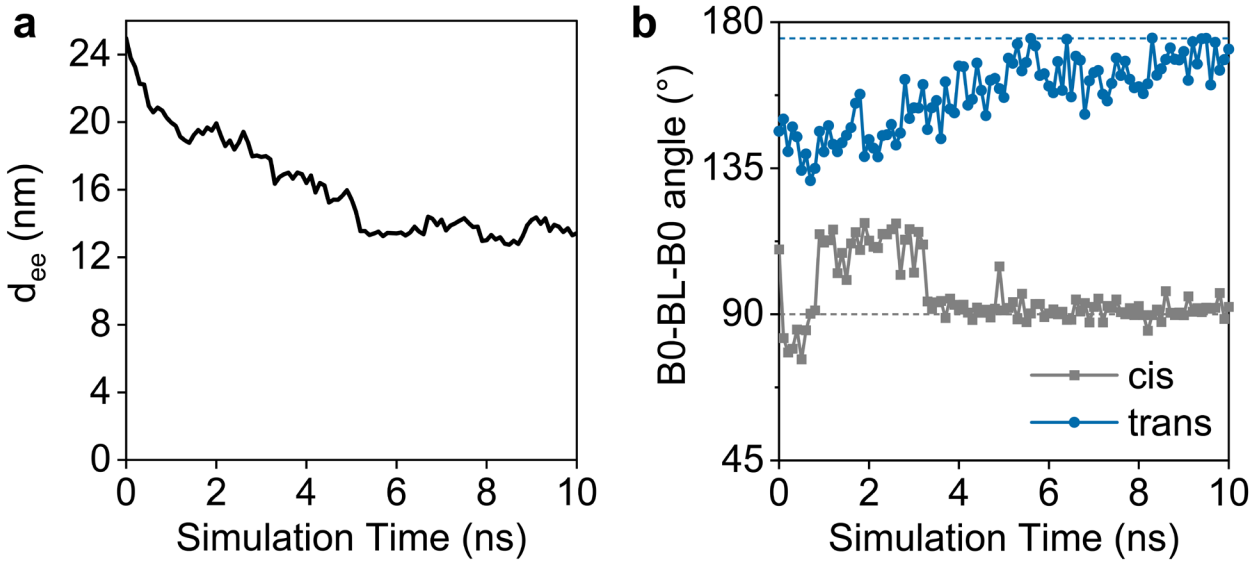

Figure S4: Atomistic equilibration of a P5 polymer (**Figure 2b**) prior to CG mapping (**Figure 2c**). (a) End-to-end distance (d_{ee}) as a function of simulation time, showing collapse of the polymer from its initial fully extended conformation (~25 nm) to a compact equilibrated structure (~14 nm) over 10 ns. (b) CG mapped B0-BL-B0 angle as a function of simulation time for *cis* (gray) and *trans* (blue) alkene linker beads, converging to their respective equilibrium values of 90° and 175°, respectively (dashed lines).

Figure S5 illustrates the implementation of the upper wall restraint using the PLUMED[12] package for both equilibration (**Figure 2f**) and production (**Figure 2g**) polymer-membrane simulations as described in the '**Polymer-Membrane Simulations**' section in the main text. An upper wall restraint potential (V_{upper}) was applied between the centers-of-mass of the polymer and membrane in the *z*-direction (z) to maintain their distance within 6 nm using the following harmonic restraint bias in **Equation S1**:

$$V_{upper} = \begin{cases} k\,(z - 6\,nm)^2, & z > 6\,nm \\ 0\,, & z \leq 6\,nm \end{cases} \quad \text{(S1)}$$

where *k* is a force constant (1000 kJ mol^{-1} nm^{-2}). V_{upper} is only applied if the center-of-mass distance exceeds 6 nm. **Figure S5** shows the center-of-mass distance between a polymer and an RBC membrane (black points) relative to the upper wall restraint distance (green dashed line) during 100 ns equilibration (**Figure 2f**). This restraint maintains close proximity of the polymer to the membrane (snapshots (i) and (ii)), increasing polymer-membrane sampling and promoting faster equilibration toward bound conformations (snapshots (iii) and (iv)) prior to production simulations (**Figure 2g**).

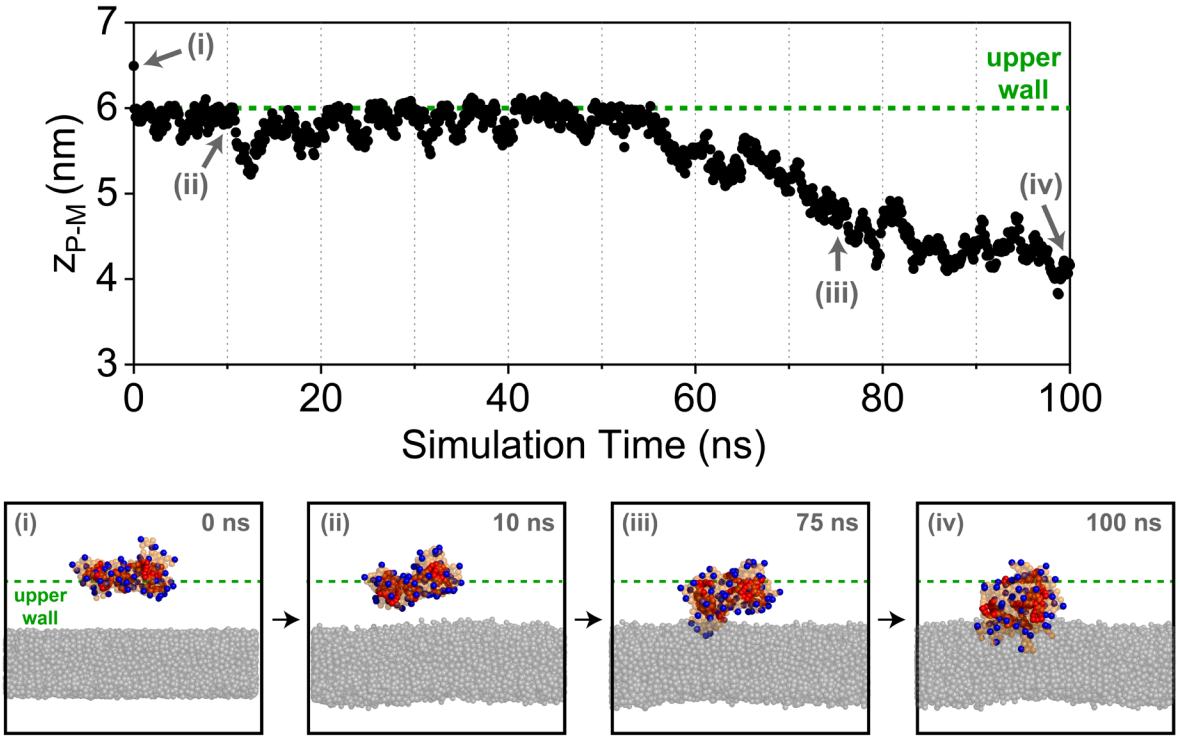

Figure S5: Implementation of the PLUMED upper wall restraint (green dashed line) on the center-of-mass distance between a polymer and RBC membrane ($z_{P\text{-}M}$, black points). Representative snapshots are provided to visualize the evolution of $z_{P\text{-}M}$ during equilibration. Membrane lipid and polymer beads are shown using the same color scheme as **Figure 4b**.

All raw R_g profiles used to generate the plots in **Figure 3d** are provided in **Figure S6**. These plots show that trends in 20-mer backbone rigidity in water as a function of *cis*/*trans* ratios discussed in the '**PONI Backbone Parameterization and Validation**' section are well-equilibrated during 50 ns production simulations across three independent replicas.

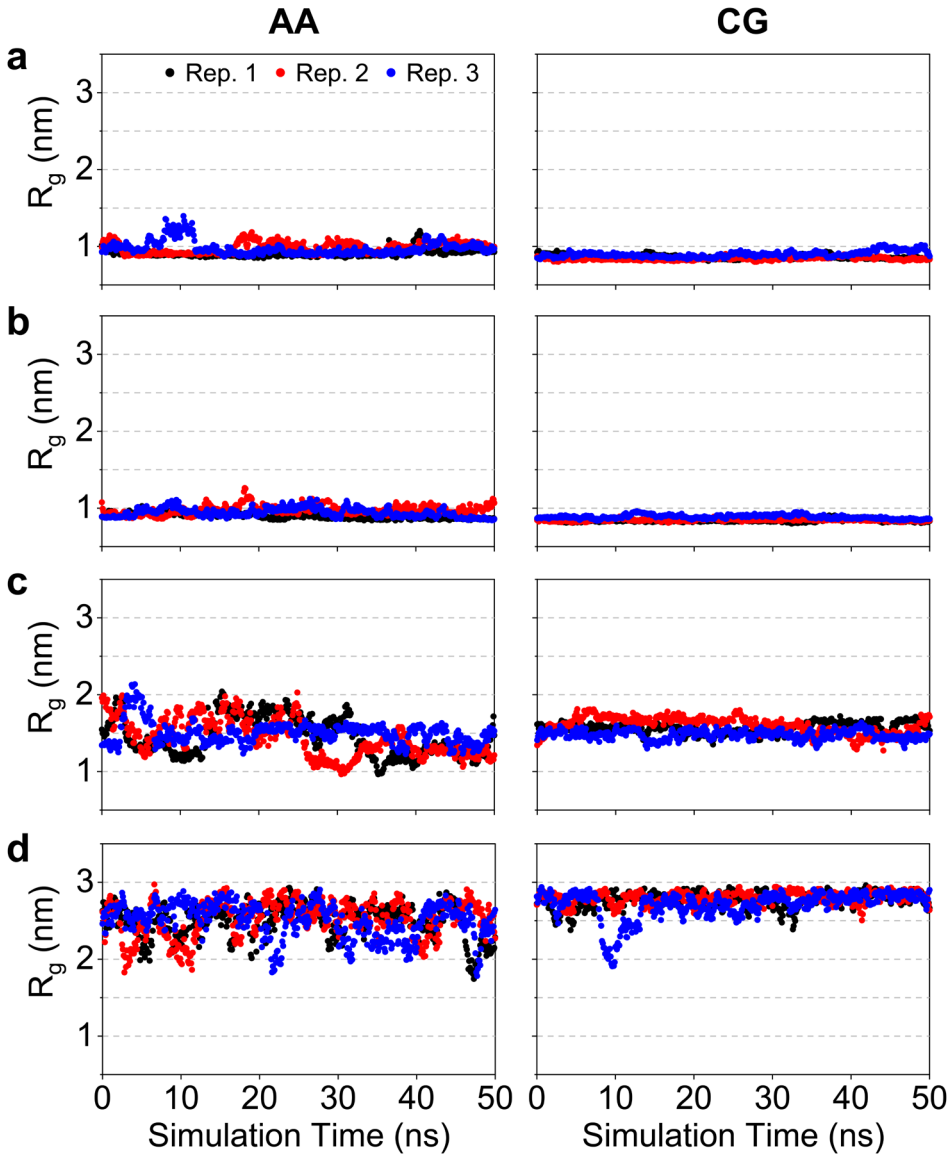

Figure S6: Raw R_g profiles from 50 ns production simulations of PONI backbone-only (a) Cis, (b) Alt, (c) Block, and (d) Trans 20-mers in water used for **Figure 3d**. All-atom (AA) results are on the left and coarse-grained (CG) results are on the right. Profiles are shown for three independent replicas: replica 1 (black), replica 2 (red), and replica 3 (blue).

We additionally compare trends in R_g across PONI architectures to differences in end-to-end distance (d_{ee}), another commonly used metric for validating conformational rigidity of coarse-grained polymer models.[13, 14] Raw d_{ee} results from the same 50 ns simulations used for **Figure S6** are shown in **Figure S7**, with replica-averaged trends across the four PONI backbone architectures (**Figure 3b**) visualized in **Figure S8**. We demonstrate that trends in d_{ee} are consistent with R_g results (**Figure 3d**), and PONI architectues targeting a ~50:50 *cis*/*trans* alkene ratio – collapsed structure of 'Alt' and more extended structure of 'Block' (**Figure 3b**) – demonstrate excellent agreement between AA and CG polymer simulations (boxed in blue in **Figure S8**).

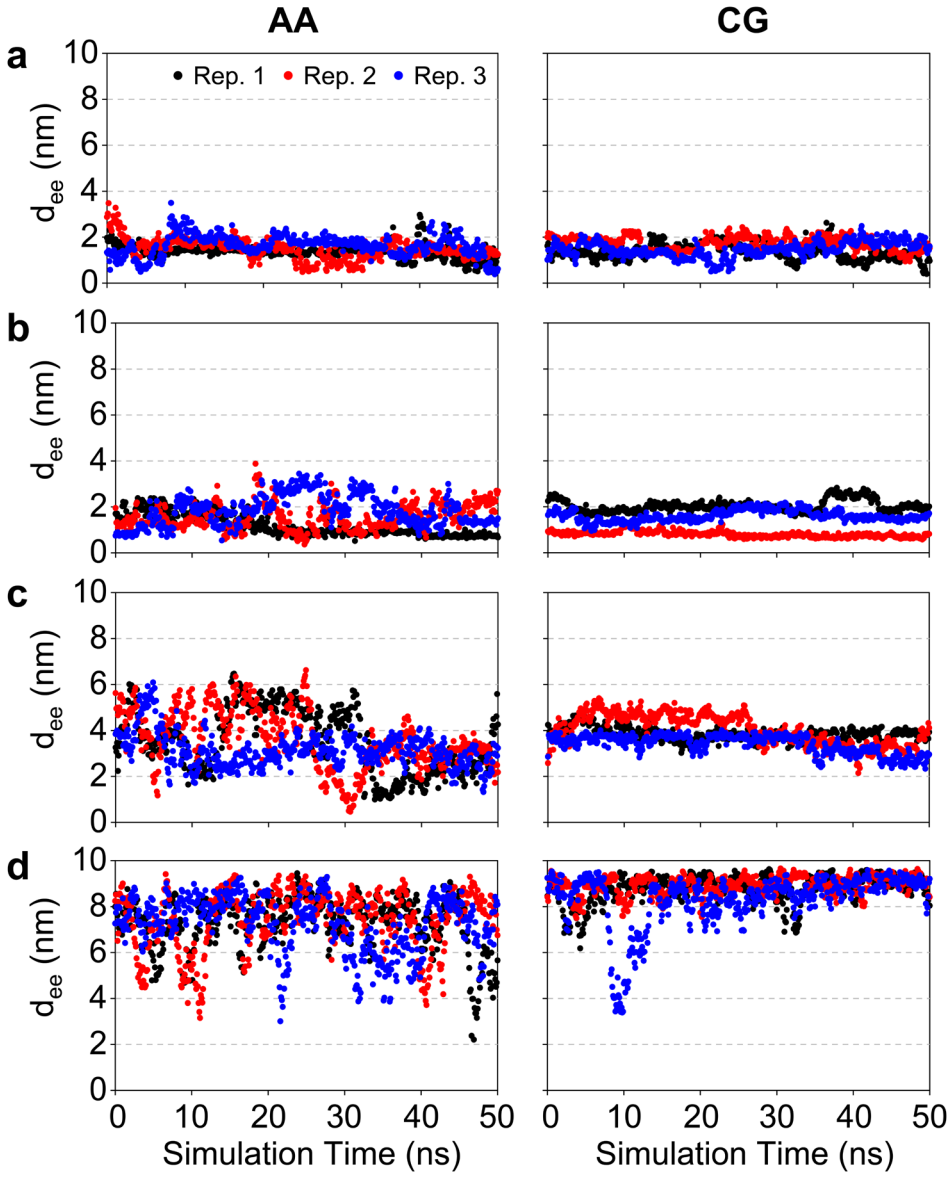

Figure S7: Raw end-to-end distance (d_{ee}) profiles from 50 ns production simulations of PONI backbone-only (a) Cis, (b) Alt, (c) Block, and (d) Trans 20-mers in water used for **Figure S8**. All-atom (AA) results are on the left and coarse-grained (CG) results are on the right. Profiles are shown for three independent replicas: replica 1 (black), replica 2 (red), and replica 3 (blue).

	AA	CG
Cis	1.49 ± 0.14 nm	1.53 ± 0.19 nm
Alt	1.53 ± 0.32 nm	1.48 ± 0.62 nm
Block	3.44 ± 0.25 nm	3.76 ± 0.32 nm
Trans	7.30 ± 0.08 nm	8.67 ± 0.32 nm

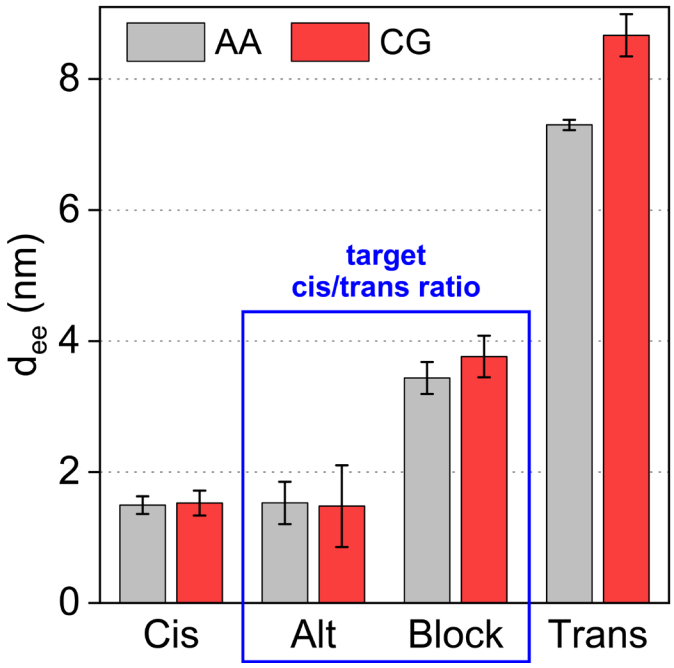

Figure S8: Replica-averaged d_{ee} results for the four 20-mer PONI architectures from AA (gray) and CG (red) simulations. Error bars indicate standard deviations across replicas. Bar chart values tabulated at the top show the average ± standard devation d_{ee} for each system.

Figures S9-S11 show all newly parameterized bonded parameters for the CG PONI backbone (**Figure 3a**): monomer parameters (**Figure S9**) and parameters between monomers across the alkene linker separately parameterized for *cis* (**Figure S10**) and *trans* (**Figure S11**) double bonds. The four beads constituting the bicyclic PONI backbone (**Figure S9a**) were parameterized with distance constraints (**Figure S9b**), consistent with previous MARTINI parameterizations of ring structures. Plots in **Figure S9b** for these five constraints demonstrate tight bond histogram distributions from mapped AA simulations (light blue) with corresponding CG distance constraints (red) based on average values across the four PONI backbones for 20-mers in water (**Figure 3c**). An 180° improper dihedral (B3-B2-B1-B0, **Figure S9b**) was implemented to maintain the planarity of these beads observed from atomistic simulations in water. All non-bonded interactions between PONI backbone beads (**Figure S9a**) were excluded as recommended by MARTINI 3 for rigid molecular fragments.[15]

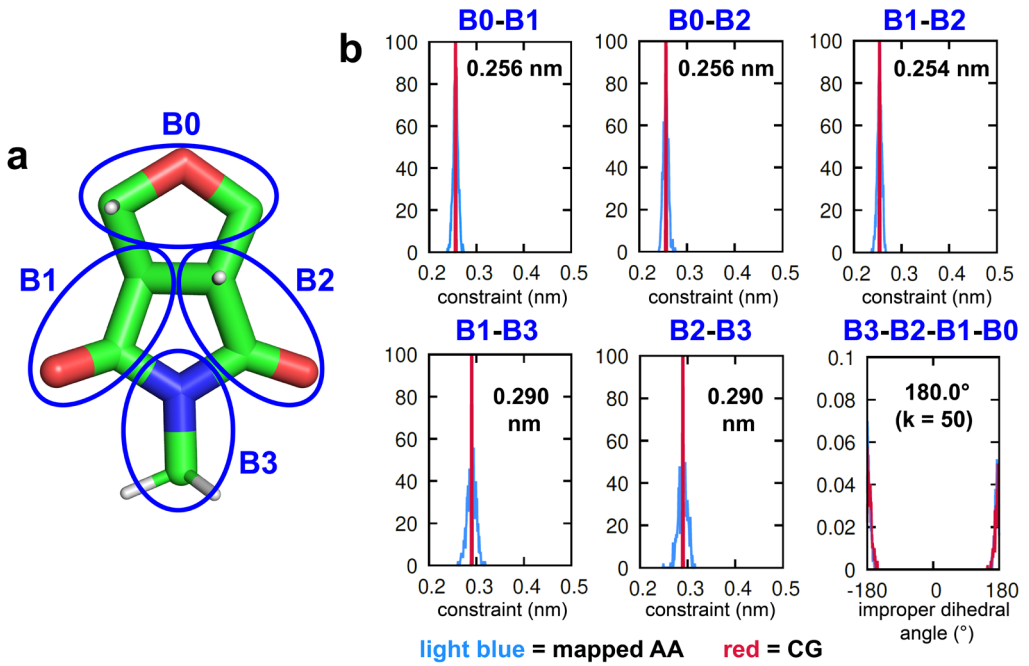

Figure S9: CG parameterization of bonded interactions for PONI backbone monomers. (a) AA-to-CG mapping strategy following **Figure 3a**, with unique bead names for the four bicyclic backbone beads (B0-B3). (b) Comparison of bonded distributions from mapped AA (light blue) and CG (red) simulations for five distance constraints (B0-B1, B0-B2, B1-B2, B1-B3, B2-B3) and one improper dihedral angle (B3-B2-B1-B0) implemented in the CG model.

To accurately capture the conformational behavior of CG PONI models for different *cis*/*trans* distributions (**Figures 3b-c**), we parameterized bonded interactions across the alkene double bond (labeled 'BL') separately for *cis* (**Figure S10**) and *trans* (**Figure S11**) isomers. This resulted in different equilibrium and force constant (labeled 'k') values set for the same bonds and angles between adjacent monomers (first two rows in **Figures S10b**, **S11b**). Additionally, two 0° proper dihedral restraints (B3-B2-B0-BL and BL-B0-B1-B3) were implemented for both *cis* and *trans* isomers to maintain planarity of bicyclic monomer units with alkene double bonds. All non-bonded interactions between the 'BL' bead and adjacent backbone monomer beads were also excluded.

For *trans* isomers (**Figure S11**), an additional 90° proper dihedral restraint for B2-B0-BL-B1 (together with an angle restraint set at 127° for B0-BL-B1) was required to accurately reproduce torsional behavior of *trans* backbone units observed in atomistic simulations (**Figure 3c**). Lastly, to capture the enhanced rigidity of *trans* chains seen in the 'Block' and 'Trans' PONI architectures (**Figure 3c**), we implemented a moderately stiff BL-BL-BL angle restraint at 175° for all sets of three consecutive *trans* alkene double bonds (visualized in **Figure S11a**).

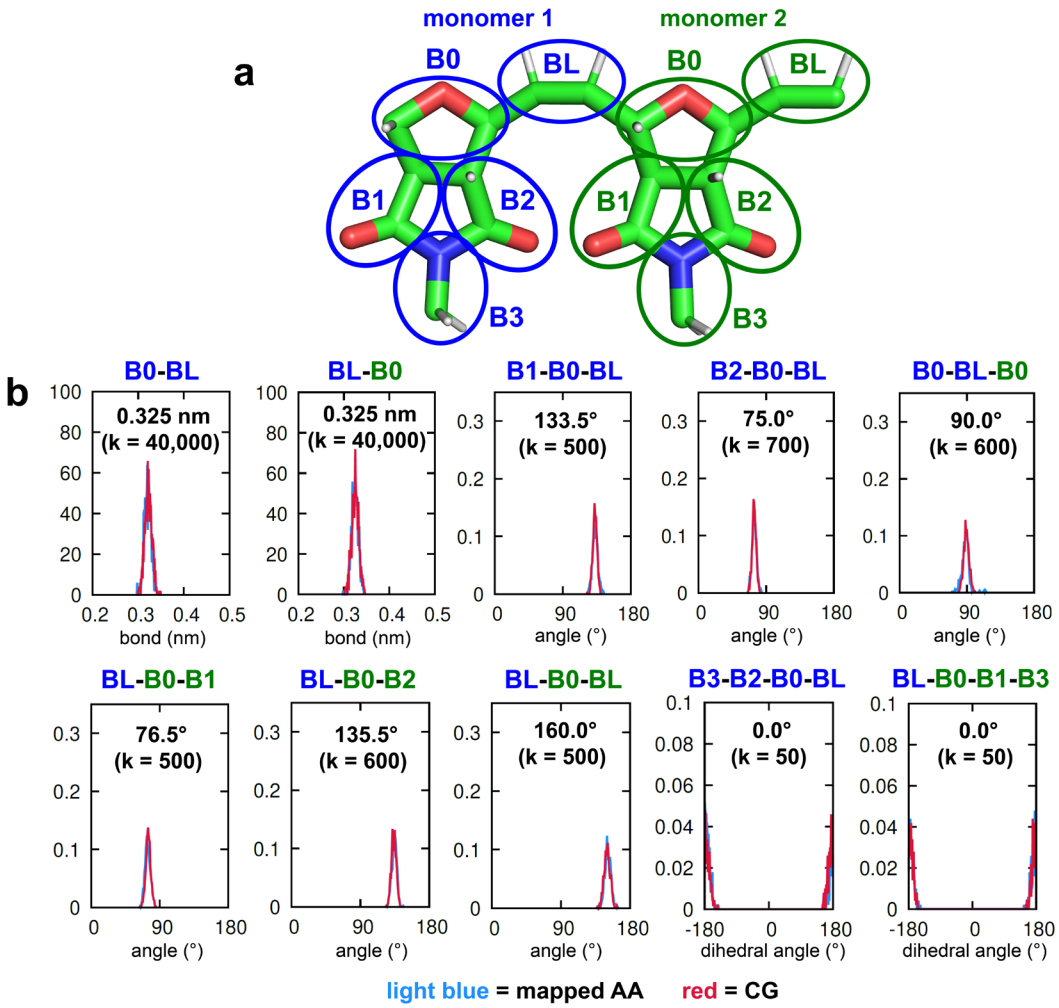

Figure S10: CG parameterization of bonded interactions involving *cis* alkene double bonds. (a) AA-to-CG mapping strategy following **Figure 3a**, with unique bead names for the four bicyclic backbone beads (B0-B3, same as **Figure S9**) and the *cis* double bond (BL). (b) Comparison of bonded distributions from mapped AA (light blue) and CG (red) simulations for all bonds (two beads), angles (three beads), and proper dihedrals (four beads) implemented in the CG model.

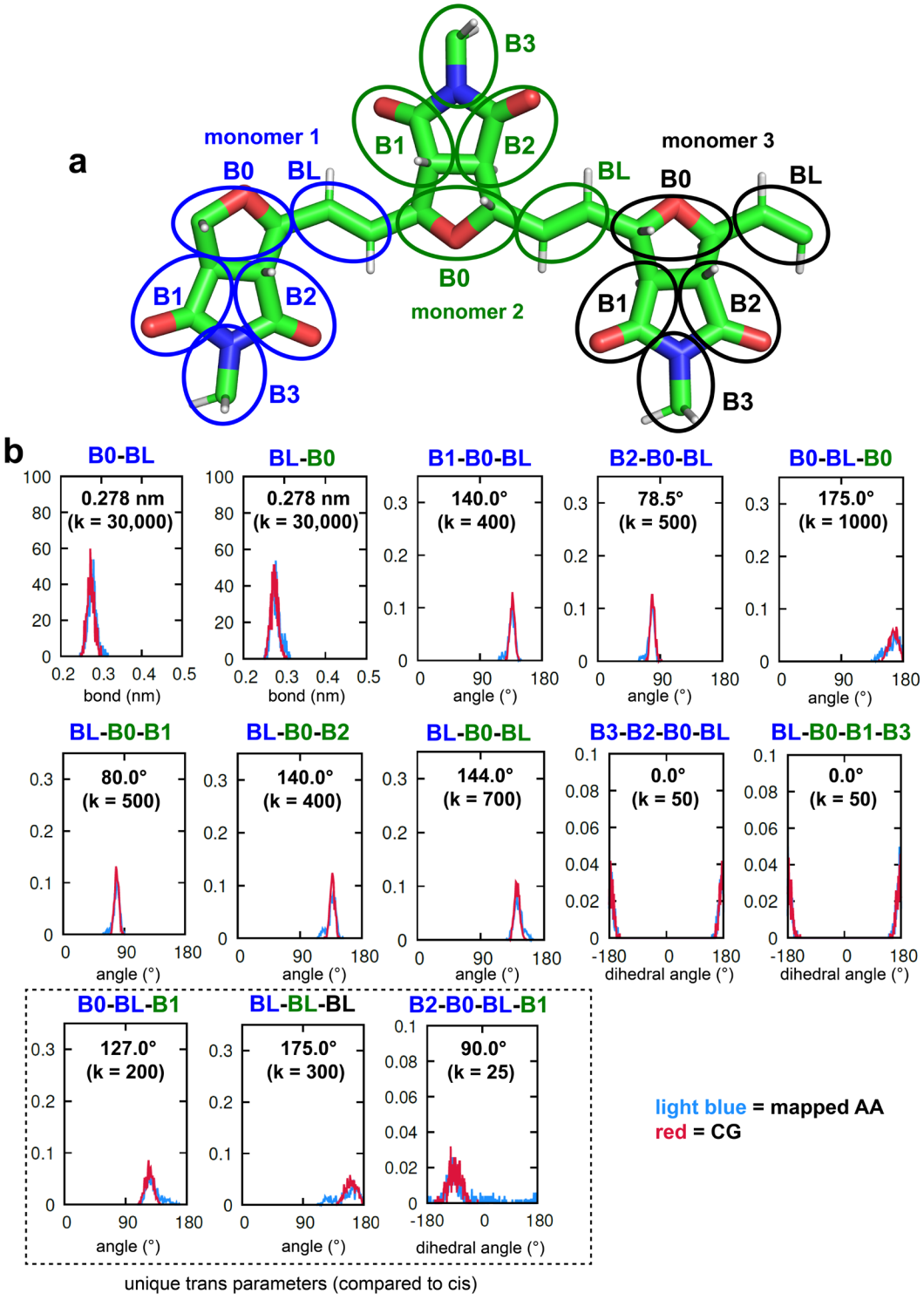

Figure S11: CG parameterization of bonded interactions involving *trans* alkene double bonds. (a) AA-to-CG mapping strategy following **Figure 3a**, with unique bead names for the four bicyclic backbone beads (B0-B3, same as **Figure S9**) and the *trans* double bond (BL). (b) Comparison of bonded distributions from mapped AA (light blue) and CG (red) simulations for all bonds (two beads), angles (three beads), and proper dihedrals (four beads) implemented in the CG model.

To validate the non-bonded interactions of the MARTINI 3 model for the oxanorborneneimide backbone, we computed water-octanol partitioning free energy profiles from both atomistic (CHARMM36) and coarse-grained (MARTINI 3) umbrella sampling simulations. This four-bead fragment for the bicyclic backbone ring (**Figure 3a**) carries the greatest non-bonded parameterization uncertainty of the PONI monomer, as it contains electronically coupled functional groups in close proximity (e.g., two carbonyl groups flanking a tertiary amine) that are mapped as isolated moieties in MARTINI 3.

The initial simulation system consisted of the PONI backbone fragment centered in a water box with an octanol box of equal dimensions appended in the positive *z*-direction. Atomistic simulations contained 1193 water and 150 octanol molecules and coarse-grained simulations contained 473 W beads (equivalent to 1892 water molecules) and 220 octanol molecules. The coarse-grained system was ~50% larger overall to ensure converged bulk water and octanol regions for free energy analysis, as the less distinct water-octanol phase barrier in the coarse-grained system allows octanol to diffuse into the water phase. Umbrella sampling simulations utilized the same parameters described for single PONI polymer *NPT* production simulations in water in the main text, except semi-isotropic pressure coupling was applied with the *x* and *y* box dimensions fixed at 3.0 nm. Windows were spaced at 0.1 nm increments with a harmonic force constant of 1000 kJ mol^{-1} nm^{-2} to restrain the PONI backbone fragment center-of-mass (COM) along the *z*-axis. Atomistic simulations used 46 windows from z = 2.0 to 6.5 nm with 20 ns of sampling per window, and coarse-grained simulations used 69 windows from z = 3.2 to 10.0 nm with 70 ns of sampling per window. Potential of mean force (PMF) profiles were constructed with Grossfield's implementation of the weighted histogram analysis method (WHAM).[16]

Figure S12 shows the results of atomistic (**Figure S12a**) and coarse-grained (**Figure S12b**) umbrella sampling simulations for the oxanorborneneimide backbone fragment. Both PMF profiles demonstrate similar features, including a free energy minimum at the water-octanol interface (snapshot (ii)) and a lower free energy in bulk octanol (snapshot (iii)) compared to bulk water (snapshot (i)), indicating a clear thermodynamic preference for partitioning into the hydrophobic phase. Quantitatively, the difference between the PMF for plateau values in the water phase and octanol phase (*i.e.*, the water-octanol partitioning free energy) calculated from the two models agree within ~4 kJ mol^{-1} (~1.6 k_BT), which is within the expected accuracy of the MARTINI 3 framework (deviations up to 5.7 kJ mol^{-1} relative to experiment for common small molecules).[17] Together, these results support the reliability of the chosen bead mapping (**Figure 3a**) in capturing the net hydrophobic character of the oxanorborneneimide backbone.

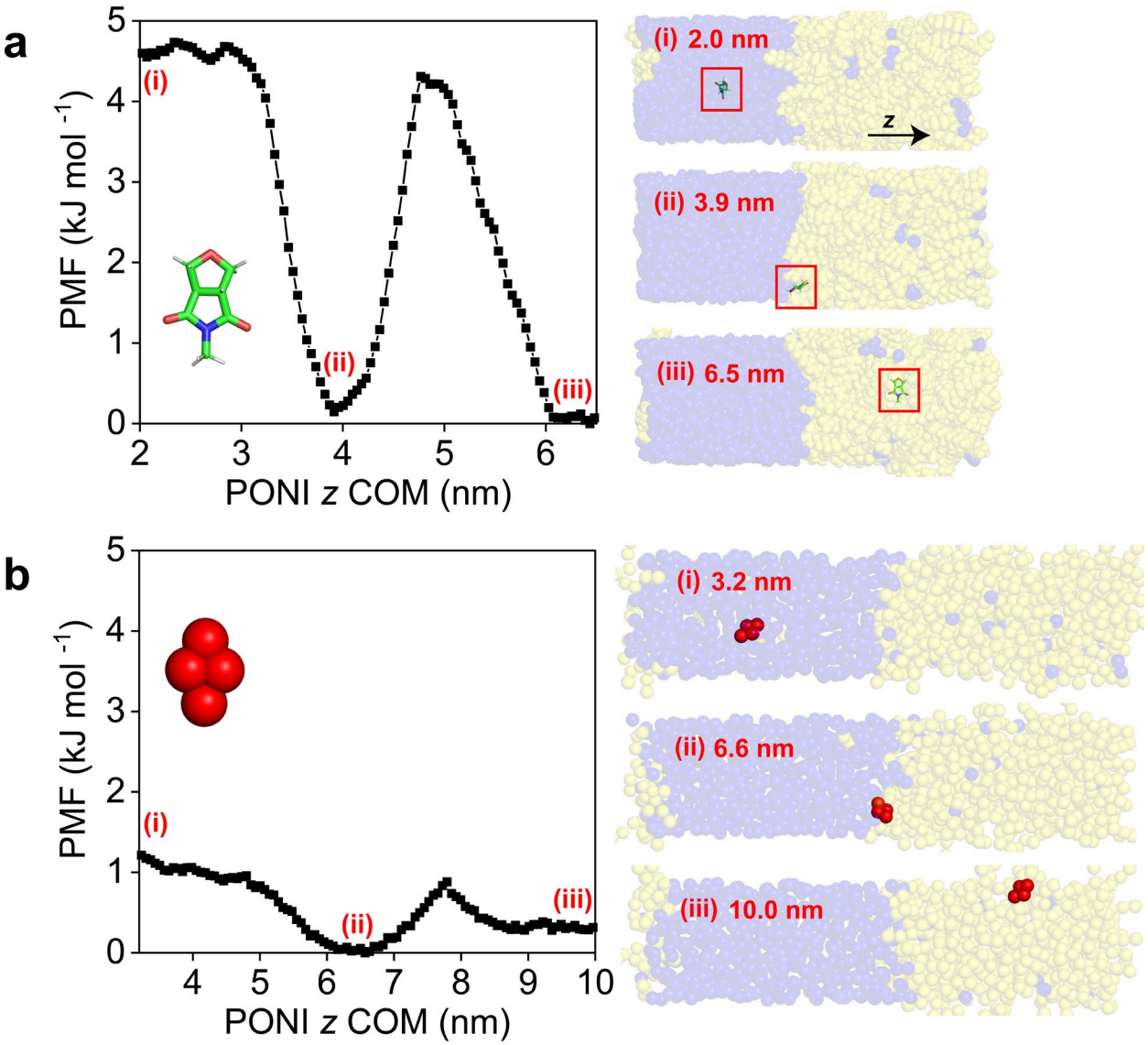

Figure S12: Water-octanol partitioning free energy profiles for the oxanorborneneimide backbone fragment from (a) atomistic and (b) coarse-grained umbrella sampling simulations. PMF profiles (black points) were computed using Grossfield's implementation of WHAM with 100 bins. Representative snapshots show the fragment in bulk water (i), at the water-octanol interface (ii), and in bulk octanol (iii), which are inset on the PMF plots. The backbone fragment is shown as sticks (atomistic) or red beads (coarse-grained). Water and octanol molecules are shown as transparent blue and yellow spheres, respectively.

Figure S13 shows the bonded interactions parameterized for all four PONI polymer side chains (**Figure 1a**) as described in the '**PONI Side Chain Parameterization and Bacterial vs. RBC Membrane Interaction Behavior**' section in the main text. All parameters are provided as .ff files compatible with the polyply python suite[18] for use in automated construction of randomized polymer architectures modeled in this study. The P1 side chain was parameterized with a stiff bond (k = 50,000 kJ mol^{-1} nm^{-2}) between the backbone B3 bead (**Figure S9a**) and the side chain quaternary ammonium (QA) group (**Figure S13a**). The remaining PONI side chains (P3, P5, P9) were parameterized with a combination of weaker bonds (k = 5000 kJ mol^{-1} nm^{-2}) and 180° angles to reflect the linear geometry of alkyl chains (**Figures S13b-d**), with an additional 90° angle applied to A2-QA-R1 in the P9 side chain (**Figure S13d**) to capture the right-angle geometry of a quaternary ammonium with alkyl chains on either side.

The B3-A1 bond parameterized for the P3 side chain (**Figure S13b**) was also utilized for the P5 and P9 side chains (**Figures S13c-d**). The A1-A2 bond, A2-QA bond, B3-A1-A2 angle, and A1-A2-QA angle parameterized for the P5 side chain (**Figure S13c**) were also utilized for the P9 side chain (**Figure S13d**).

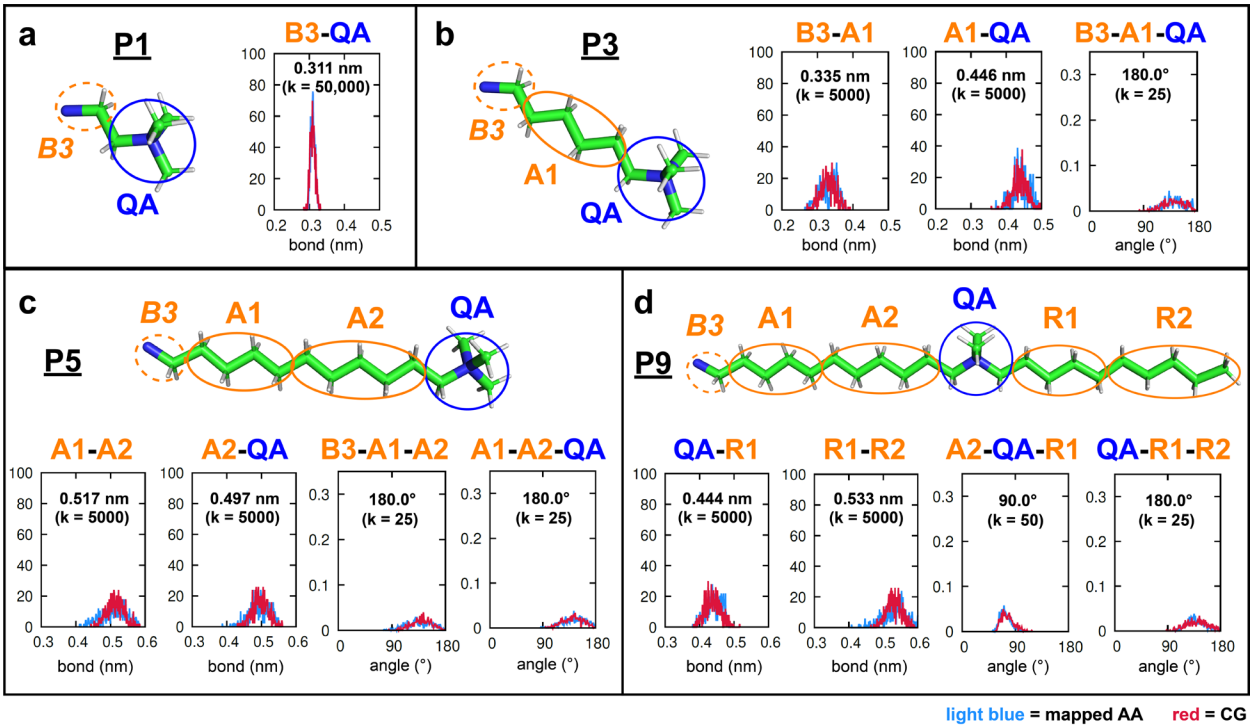

Figure S13: CG parameterization of bonded interactions for all PONI polymer side chains: (a) P1, (b) P3, (c) P5, and (d) P9. AA-to-CG mapping strategies follow **Figure 4a**, with unique bead names for linear alkyl segments (A1, A2, R1, R2) and the quaternary ammonium group (QA). Plots compare bonded distributions from mapped AA (light blue) and CG (red) simulations for all bonds (two beads) and angles (three beads) implemented in CG models for each side chain.

Figures **S14-S15** visualize final simulation snapshots from replica 2 (**Figure S14**) and replica 3 (**Figure S15**) polymer-membrane simulations, supporting **Figure 4b** in the main text and the reproducibility of trends discussed in the '**PONI Side Chain Parameterization and Bacterial vs. RBC Membrane Interaction Behavior**' section. Specifically, the following behaviors are consistent across all three replicas, independent of the *cis*/*trans* distribution along the polymer backbone randomized across replicas:

1. P3 polymers adopt more extended conformations in bacterial (*E. coli*, MRSA) membranes compared to P1 while remaining surface bound.
2. P5 and P9 polymers insert into bacterial membranes, with increased lower leaflet anchoring of quaternary ammonium groups (blue beads) displayed in MRSA vs. *E. coli* membranes.
3. P1 polymers reversibly bind to RBC membranes.
4. P3 and P5 polymers irreversibly bind to RBC membranes without significant insertion.
5. P9 polymers substantially insert into RBC membranes.

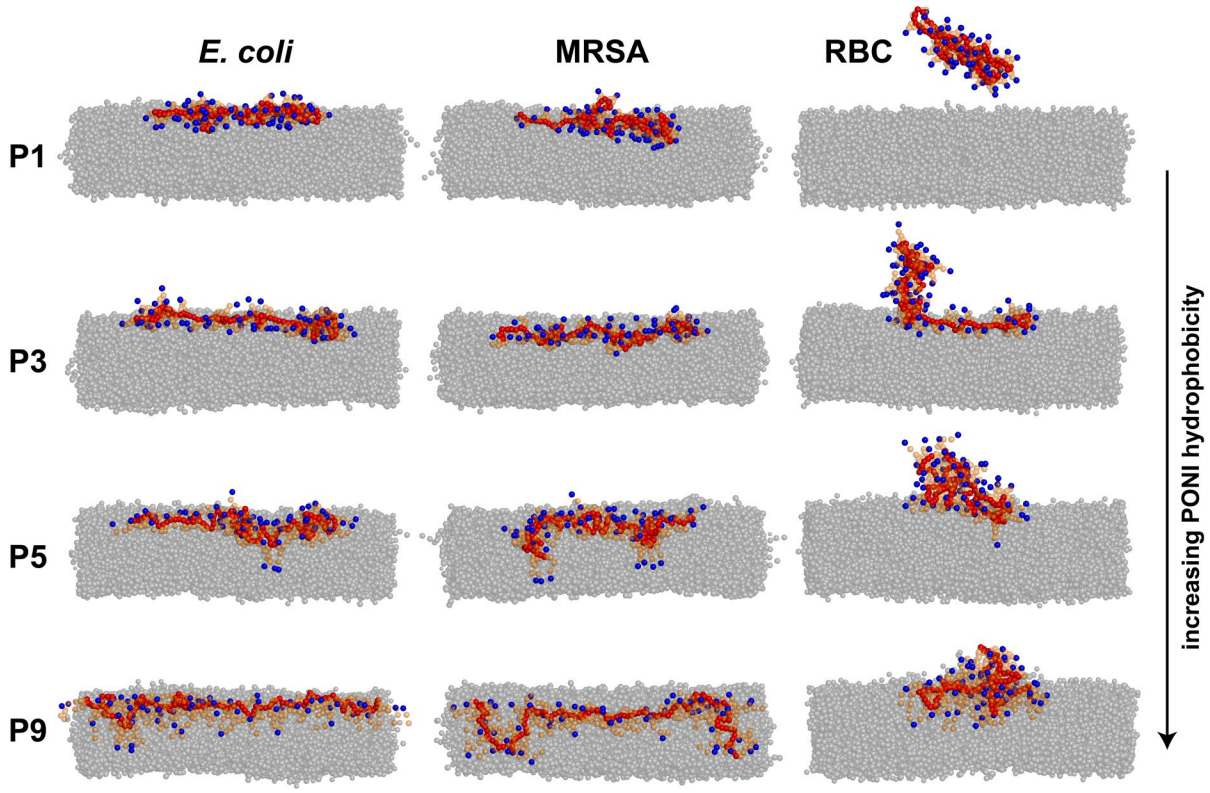

Figure S14: Final snapshots from replica 2 polymer-membrane simulations, supporting **Figure 4b** in the main text. PONI backbones are represented as opaque red and transparent orange spheres, side chains as transparent orange and opaque blue spheres, and membrane lipids as transparent gray spheres. Water and ions are omitted for clarity.

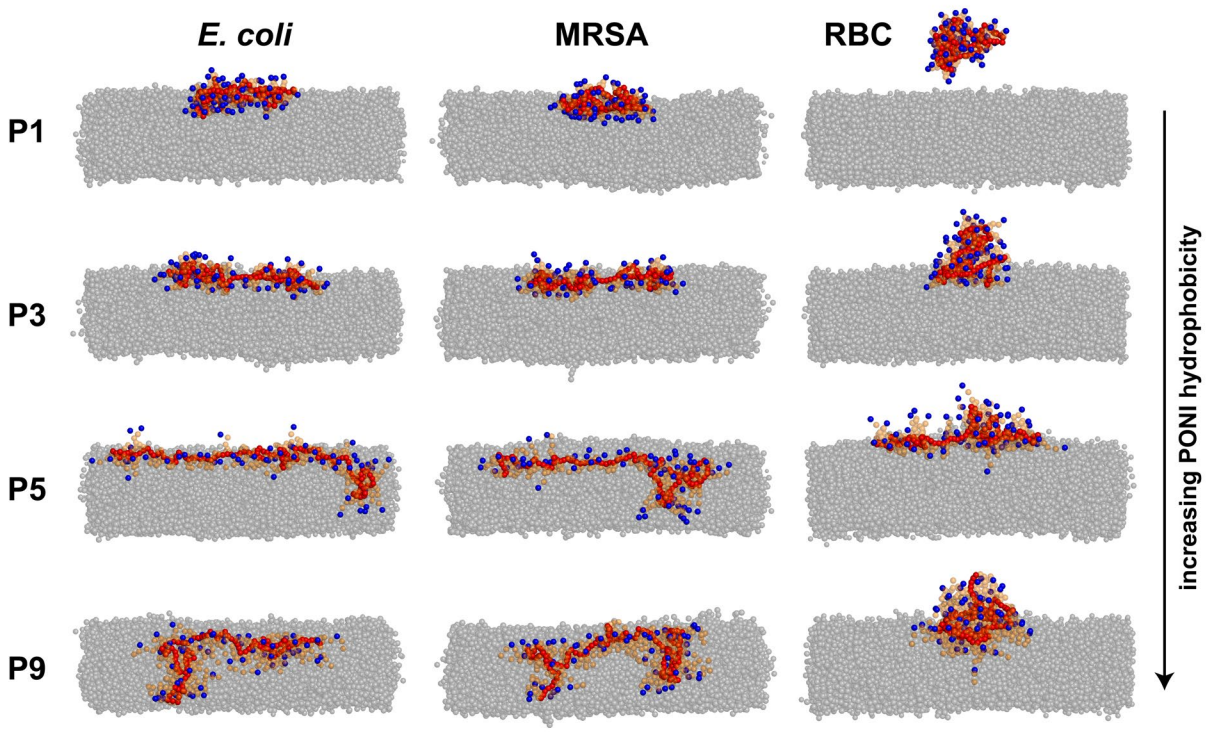

Figure S15: Final snapshots from replica 3 polymer-membrane simulations, supporting **Figure 4b** in the main text. PONI backbones are represented as opaque red and transparent orange spheres, side chains as transparent orange and opaque blue spheres, and membrane lipids as transparent gray spheres. Water and ions are omitted for clarity.

Figure S16 shows the average polymer-membrane insertion depth ($z_{P\text{-}M}$, **Figure S16a**) and radius of gyration (R_g, **Figure S16b**) for each simulation replica during the final 1 μs of sampling used to generate plots shown in **Figure 5**. These data highlight that polymer insertion depth into membranes is largely unaffected by randomized *cis*/*trans* distributions across replicas (tight distribution of $z_{P\text{-}M}$ values, **Figure S16a**), supporting that polymer insertion in membranes is primarily driven by factors such as polymer hydrophobicity and membrane lipid composition rather than polymer conformational flexibility. For example, P9 polymers utilized in our study span a broad range of backbone architectures (**Figure S17**) despite all targeting a ~50:50 *cis*/*trans* distribution. Nevertheless, all P9 replicas display consistent insertion across membrane types (**Figure S16a**), driven by their high hydrophobicity: 0.89 nm ≤ $z_{P\text{-}M}$ ≤ 1.45 nm in *E. coli*, 0.40 nm ≤ $z_{P\text{-}M}$ ≤ 0.76 nm in MRSA, and 1.87 nm ≤ $z_{P\text{-}M}$ ≤ 2.38 nm in RBC.

Similarly, polymers display narrow ranges of R_g values in bacterial membranes for side chains that remain surface bound (P1 and P3, **Figure S16b**), indicating reproducible conformational behavior across replicas. P3 polymers consistently adopt more extended conformations than P1 (reflected by larger R_g values for all three replicas), arising from increased side chain hydrophobicity that promotes lateral spreading on the membrane surface (**Figures 4b**, **S14-S15**). Conversely, in bacterial membranes, P5 and P9 side chains display large ranges in R_g values (**Figure S16b**),

primarily driven by highly extended conformations (P9 replica 2 in **Figure S14**, P5 replica 3 in **Figure S15**) with large R_g > 5 nm resulting from long *trans* segments in the polymer backbone (**Figure S17**). However, these more extended configurations do not impact their insertion capability in bacterial membranes (**Figure S16a**). In RBC membranes, all polymer side chains and replicas display collapsed structures (consistently low R_g, **Figure S16b**), which we attribute to the lack of electrostatic shielding by anionic lipids in the upper leaflet of RBC membranes compared to bacterial membranes (**Figure 8**).

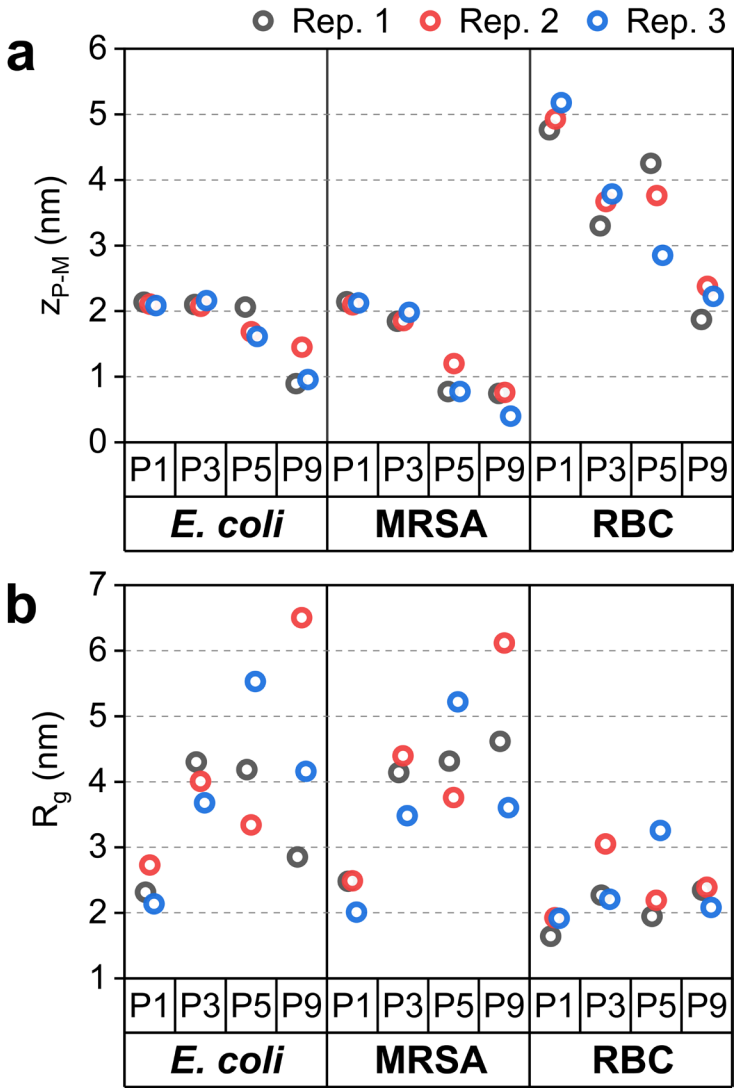

Figure S16: Average (a) polymer-membrane insertion depth (z_{P-M}) and (b) radius of gyration (R_g) calculated from the last 1 μs of three independent replicas: replica 1 (black), replica 2 (red), replica 3 (blue) used to create **Figure 5**.

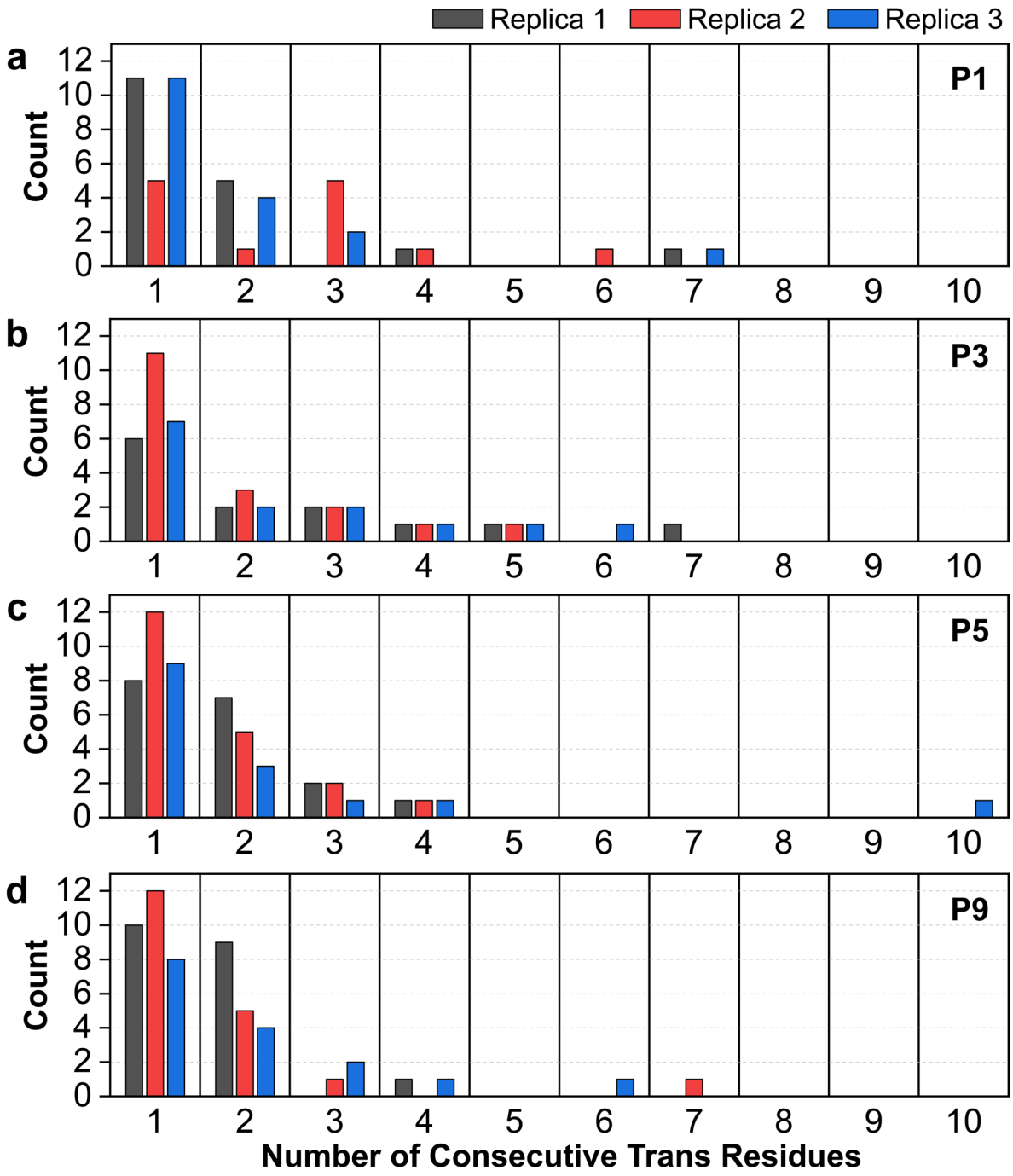

Figure S17: Backbone *trans* alkene distributions of (a) P1, (b) P3, (c) P5, and (d) P9 polymers across three independent replicas: replica 1 (black), replica 2 (red), and replica 3 (blue). Distributions show the number of consecutive *trans* residues (example of three consecutive *trans* residues in **Figure S11a**) found in each polymer.

To assess whether the relative preference for TOCL (-2 charge) versus POPG (-1 charge) enrichment differs between *E. coli* and MRSA membranes, we computed the ratio of TOCL to POPG enrichment from **Figure 8a-b** for each polymer side chain (**Figure S18**). In both membrane types, TOCL is preferentially enriched over POPG across all polymer side chains, with ratios ranging from 5.29 (P1, *E. coli*) to 1.01 (P9, MRSA). *E. coli* membranes show consistently higher TOCL/POPG enrichment selectivity ratios than MRSA across all polymer side chains, exceeding MRSA values by 38-58%. This behavior is consistent with stronger TOCL domain formation in *E. coli* observed in in-plane radial distribution functions (shown in the next section as part of **Figure S19**). Additionally, in both membranes, the TOCL/POPG enrichment selectivity ratio decreases monotonically with increasing polymer hydrophobicity, indicating that as polymers extend and insert more deeply into bacterial membranes (**Figure 5**), they lose their preference for TOCL over POPG enrichment.

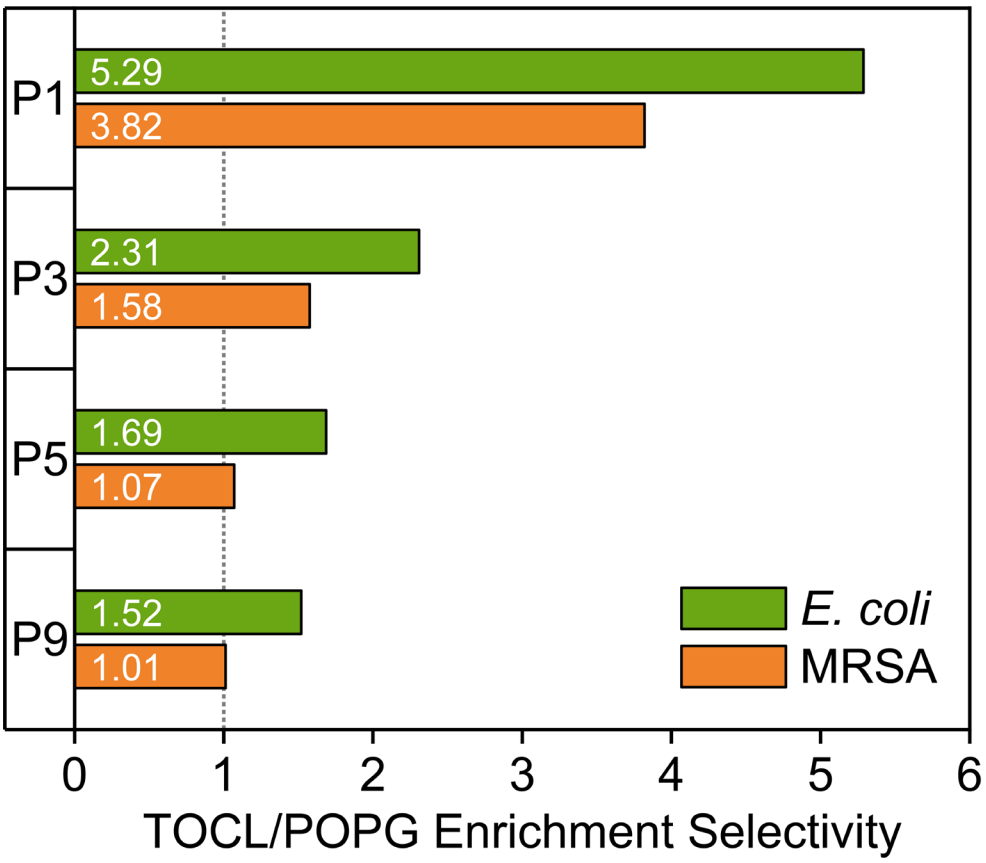

Figure S18: Ratio of TOCL to POPG enrichment for P1, P3, P5, and P9 polymers in *E. coli* (green) and MRSA (orange) membranes. Enrichment selectivity ratios greater than 1 (dashed vertical line) indicate preferential enrichment of TOCL relative to POPG.

Figures S19-S22 show lateral radial distribution functions, g(r), for each lipid type in the upper leaflet of *E. coli*, MRSA, and RBC membranes (**Figure 1b**) to support trends in polymer-lipid enrichment shown in **Figure 8**. For each lipid type, g(r) was calculated using only upper leaflet representative beads – 'PO4' bead for phospholipids, 'GLC' bead for TOCL, and 'ROH' bead for CHOL – consistent with the bead selection used in lipid enrichment analysis described in the '**Polymers Display Preferential Cardiolipin Enrichment in *E. coli* Versus MRSA Membranes**' section in the main text. Lateral radial distribution functions were computed from the last 1 μs of simulation trajectories following **Equation S2**:

$$g(r) = \frac{n(r)}{2\pi r \Delta r \rho N} \quad \text{(S2)}$$

where n(r) is the number of lipid-lipid pairs at a distance r in the *xy* membrane plane, N is the number of lipid representative beads, $\rho = N/A$ is the bulk 2D number density, A is the membrane area, and Δr is the bin width (0.02 nm). Values of g(r) > 1 indicate local lipid clustering and domain formation, while g(r) → 1 at large r indicates bulk membrane behavior.

Figure S19 shows g(r) results for TOCL lipids in bacterial *E. coli* (**Figure S19a**) and MRSA (**Figure S19b**) membranes across three independent replicas. These results highlight several key trends for TOCL lateral organization in bacterial membranes with polymers, supporting **Figure 8**:

1. P1 polymers display strong TOCL enrichment in both *E. coli* and MRSA due to recruitment by their highly collapsed, surface bound structures (low R_g, **Figure 5b**).
2. TOCL domain formation induced by P1 is consistently stronger in *E. coli* versus MRSA membranes (e.g., larger peak g(r) values defined as $g(r)_{max}$).
3. All polymers induce some degree of TOCL domain formation in *E. coli*, excluding highly extended conformations (P9 replica 2 and P5 replica 3, see **Figure S16b**), whereas only P1 induces detectable TOCL domain formation in MRSA.

To further support these observations of polymer-induced TOCL domain formation, we include g(r) profiles for POPE and POPG lipids in *E. coli* (**Figure S20**), POPGK and POPG lipids in MRSA (**Figure S21**), and all lipids and CHOL in RBC (**Figure S22**). These results show that no other lipid species exhibits domain formation in the presence of polymers compared to TOCL in bacterial membranes (**Figure S19**).

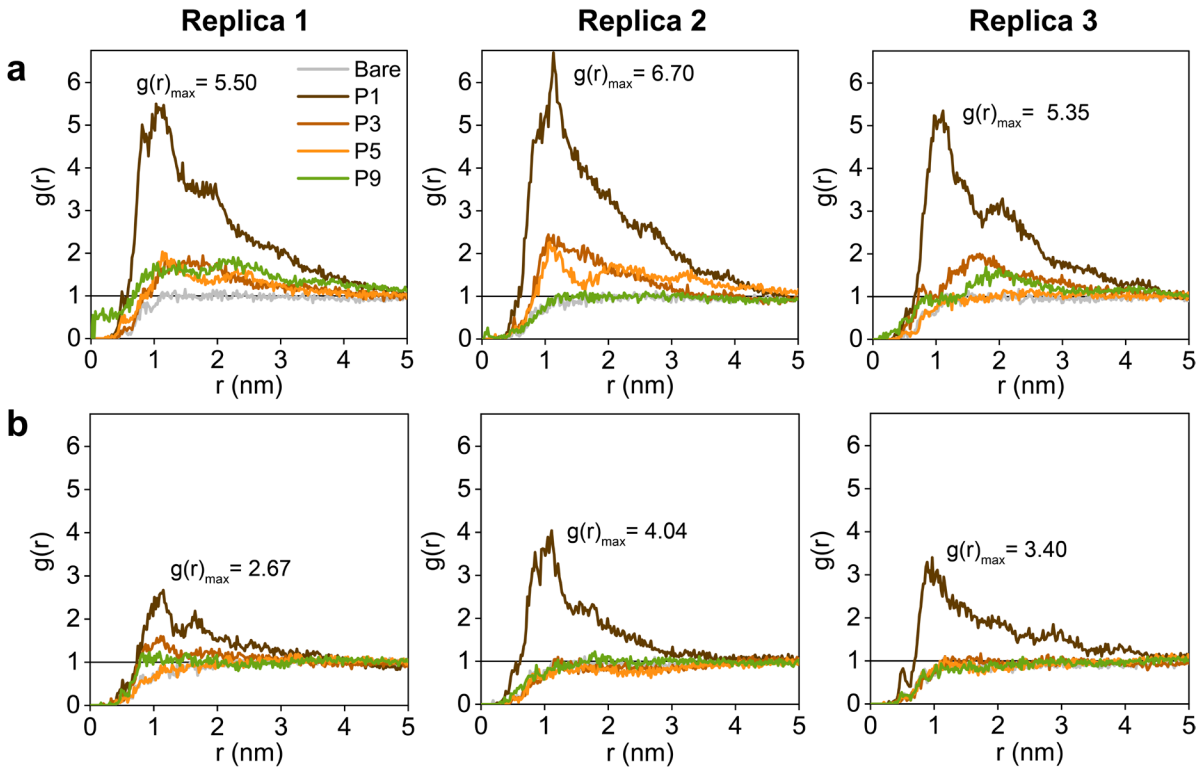

Figure S19: Lateral radial distribution functions, g(r), for upper leaflet TOCL lipids in (a) *E. coli* and (b) MRSA membranes across three independent replicas for bare membranes (gray) and membranes containing P1 (dark brown), P3 (light brown), P5 (orange), and P9 (green) polymers. Labeled $g(r)_{max}$ indicate the maximum values observed in P1 g(r) profiles.

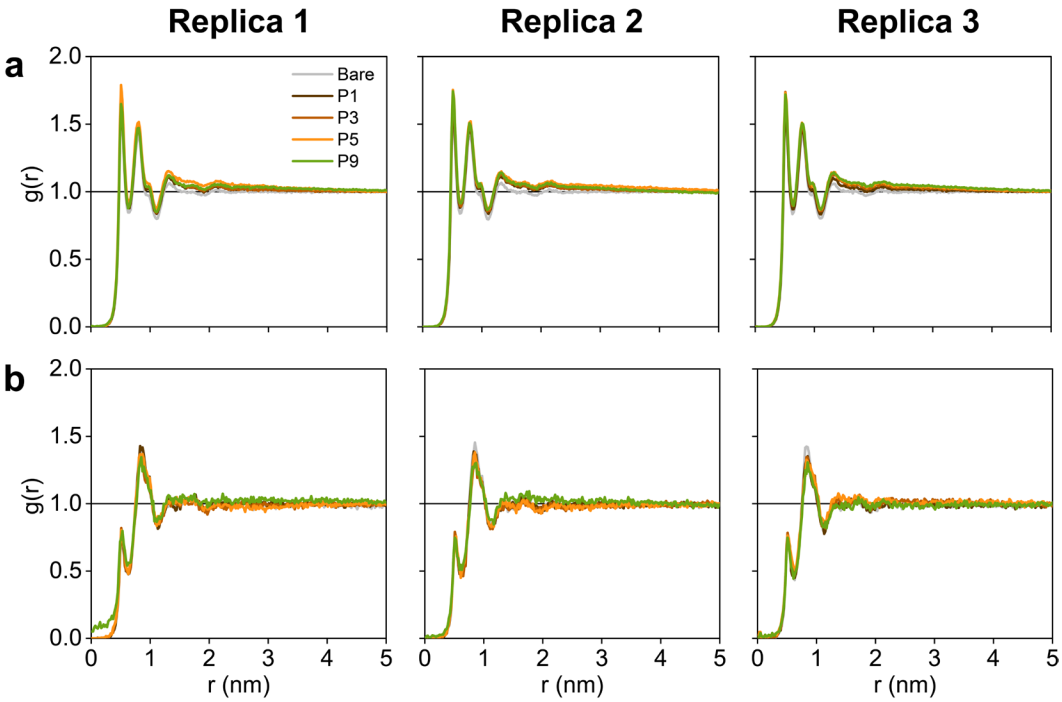

Figure S20: Lateral radial distribution functions, g(r), for upper leaflet (a) POPE and (b) POPG lipids in *E. coli* membranes across three independent replicas for bare membranes (gray) and membranes containing P1 (dark brown), P3 (light brown), P5 (orange), and P9 (green) polymers.

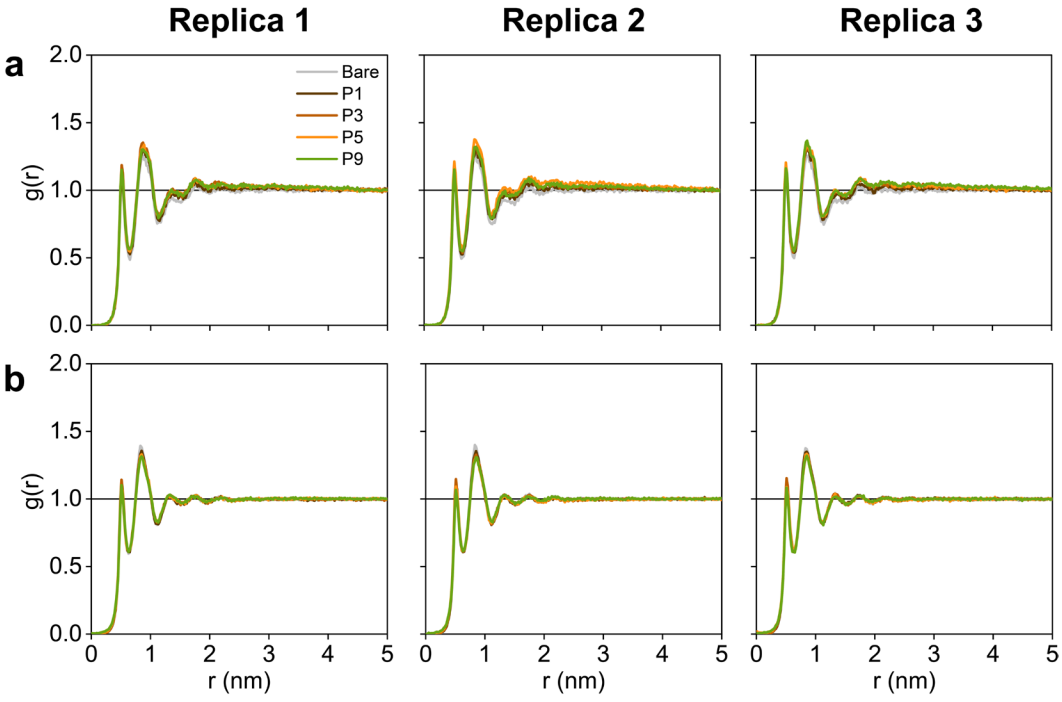

Figure S21: Lateral radial distribution functions, g(r), for upper leaflet (a) POPGK and (b) POPG lipids in MRSA membranes across three independent replicas for bare membranes (gray) and membranes containing P1 (dark brown), P3 (light brown), P5 (orange), and P9 (green) polymers.

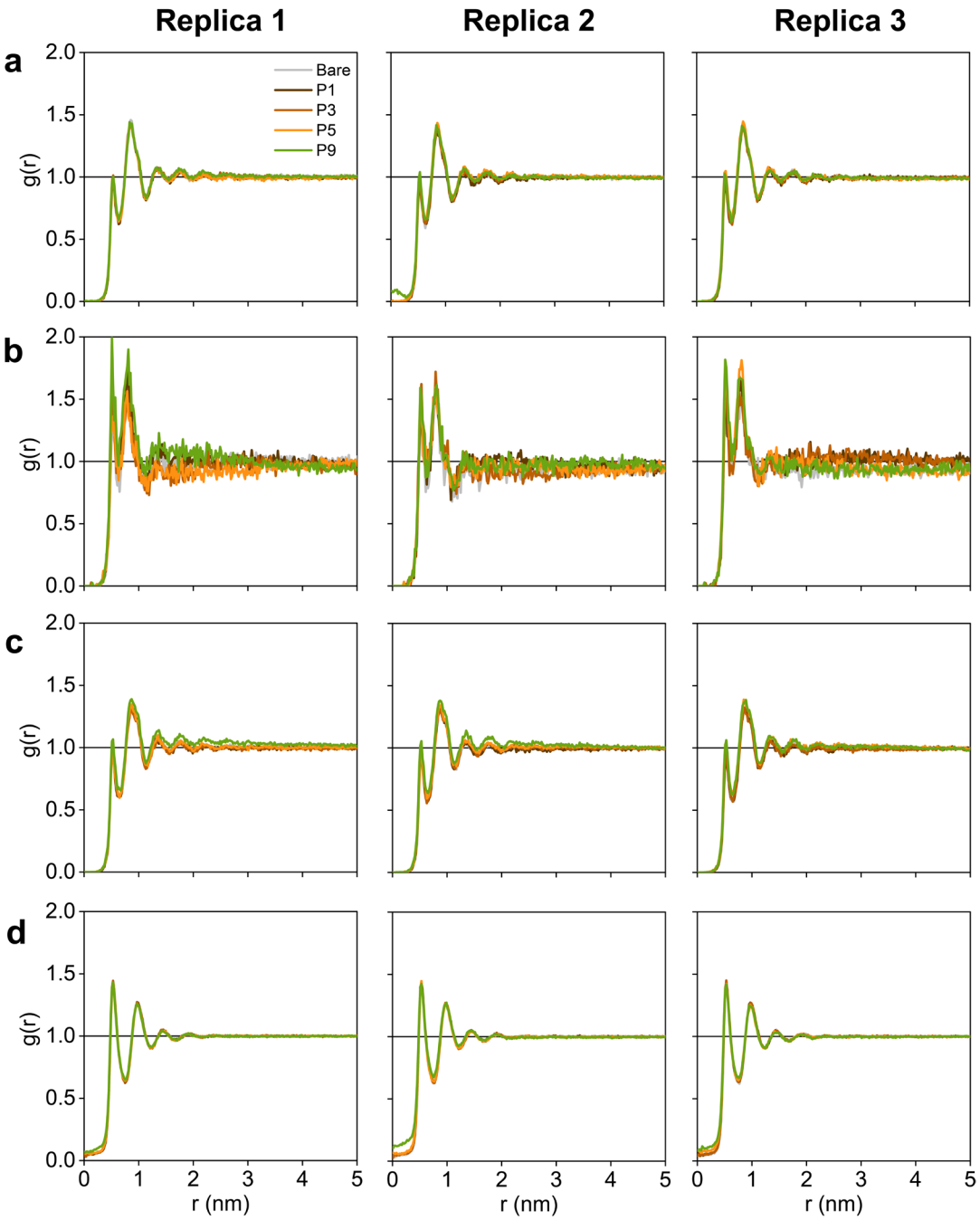

Figure S22: Lateral radial distribution functions, g(r), for upper leaflet (a) POPC, (b) POPE, and (c) POSM lipids and (d) CHOL in RBC membranes across three independent replicas for bare membranes (gray) and membranes containing P1 (dark brown), P3 (light brown), P5 (orange), and P9 (green) polymers.

Figures S23-S24 show number density profiles of lipid headgroup beads – 'PO4' for phospholipids, 'GLC' for TOCL – in the membrane hydrophobic core of *E. coli* (**Figure S23**) and MRSA (**Figure S24**) membranes in the presence of disruptive P5 and P9 polymers. Densities were calculated using 100 slices in the *z*-direction centered at the membrane center-of-mass (z = 0 nm) using the last 1 μs of each replica.

These results support the following key observations from the main text:

1. In *E. coli*, P5 fails to enrich lipids into the hydrophobic core (**Figure S23a**) due to low polymer QA density (**Figure 7a**), resulting in minimal water defect formation (**Figure 7b**).
2. In *E. coli*, a highly collapsed P9 conformation (replica 1, R_g = 2.85 nm) that produces a large water defect (n_W = 5.45, **Figure 7b**) is lined by elevated densities of POPG and TOCL (black curves in **Figure S23b**) relative to other P9 conformations.
3. In MRSA, TOCL membrane densities for P5 and P9 (**Figure S24**) are more similar across replicas compared to *E. coli* (**Figure S23**), consistent with smaller differences in pore defect sizes between these polymers in MRSA (**Figure 7b**).

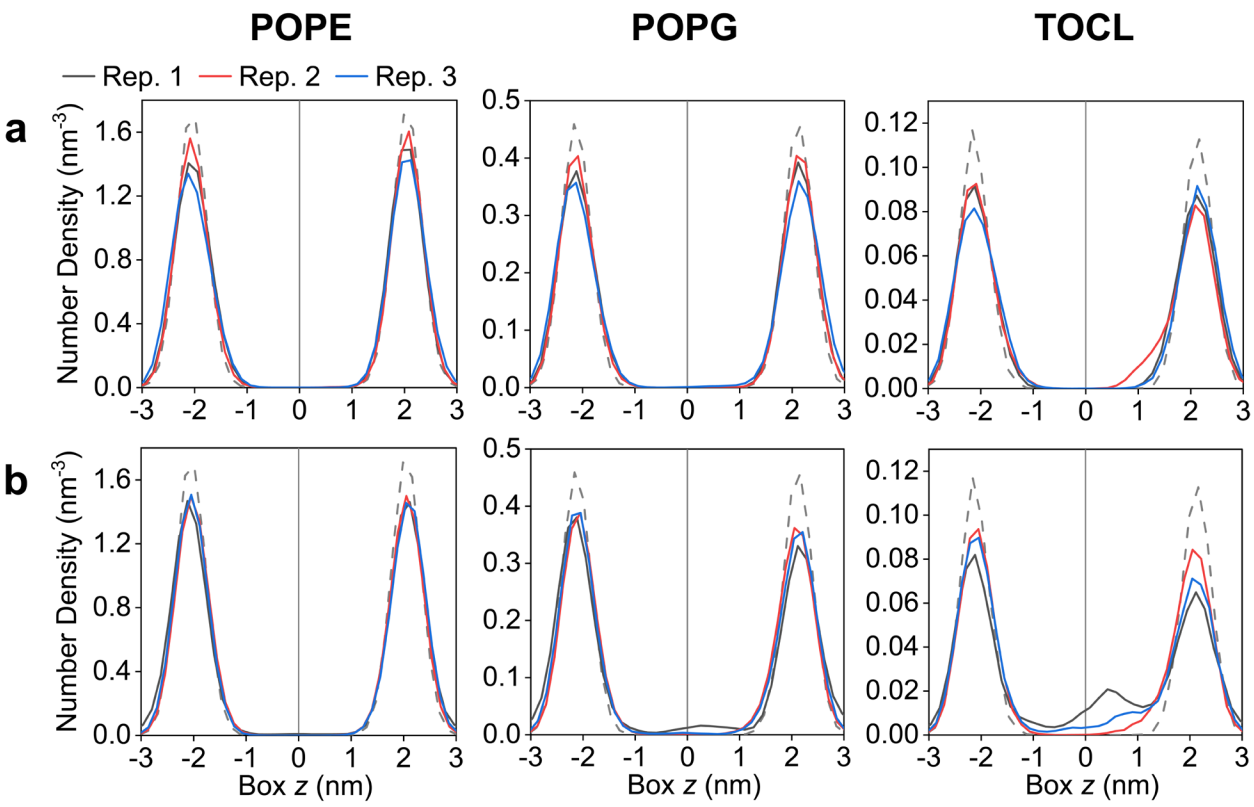

Figure S23: Number density profiles for POPE, POPG, and TOCL headgroup beads in the *z* box direction centered at the membrane center-of-mass (z = 0) for *E. coli* membranes. Results are shown for three independent replicas of (a) P5 and (b) P9 polymer systems, with a corresponding reference bare membrane profile included for each lipid type as a dashed gray plot.

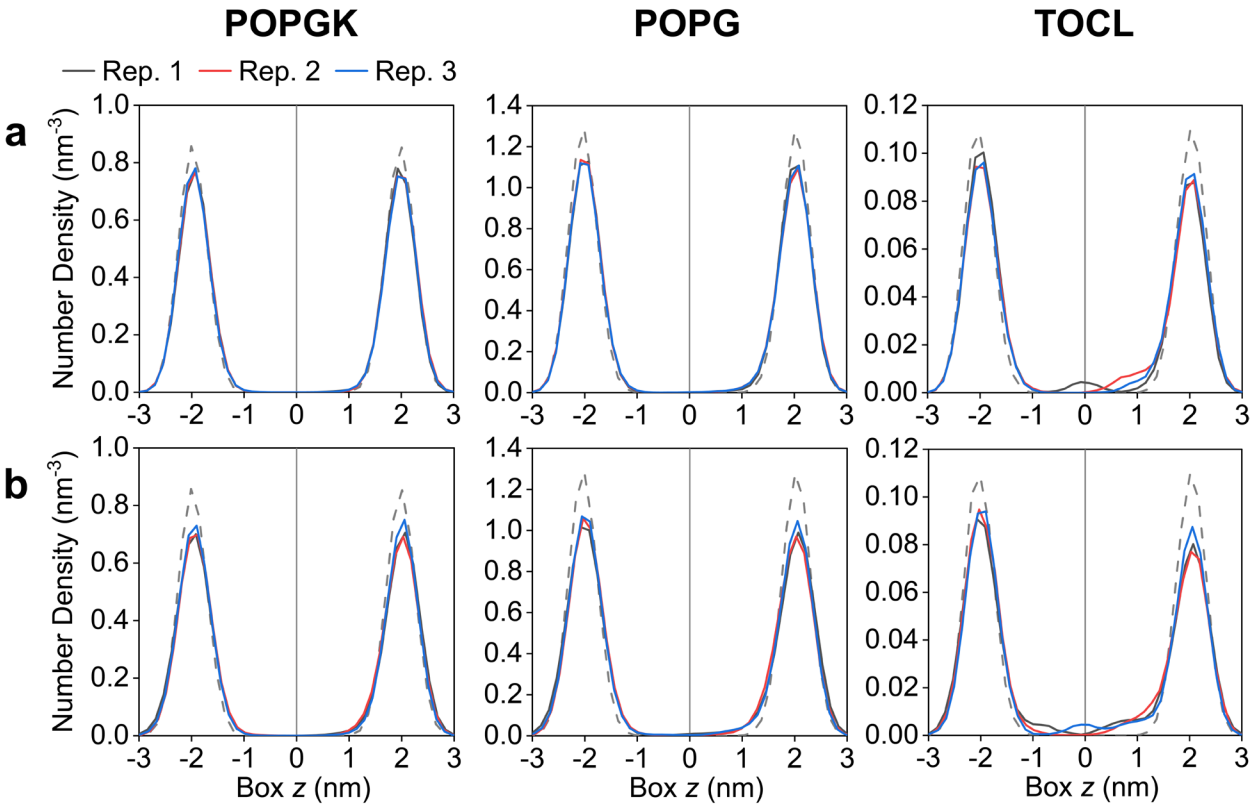

Figure S24: Number density profiles for POPGK, POPG, and TOCL headgroup beads in the *z* box direction centered at the membrane center-of-mass ($z = 0$) for MRSA membranes. Results are shown for three independent replicas of (a) P5 and (b) P9 polymer systems, with a corresponding reference bare membrane profile included for each lipid type as a dashed gray plot.

To assess whether polymer-induced membrane disruption could drive lipid flip-flop in RBC membranes, we tracked the upper leaflet fraction of each lipid species (POPC, POSM, POPE, POPS) over the 5 μs polymer-membrane production simulations across all four PONI polymer side chains and three independent replicas per polymer. We define the 'Upper Leaflet Lipid Fraction' for each lipid type as the number of lipids whose phosphatidyl PO4 bead was located above the membrane center-of-mass along the *z*-axis, normalized by the total number of that lipid type in the membrane. The lipid fractions remained constant throughout all simulations, confirming that no flip-flop events occurred even for the most disruptive polymer, P9, despite its significant membrane perturbation (**Figures 6c**, **8c**). Results for P9 are shown in **Figure S25**. This behavior is consistent with the absence of continuous transmembrane water defect formation in all polymer simulations in RBC (**Figure 7b**), which we previously identified as a necessary condition for lipid translocation in RBC membranes.[6]

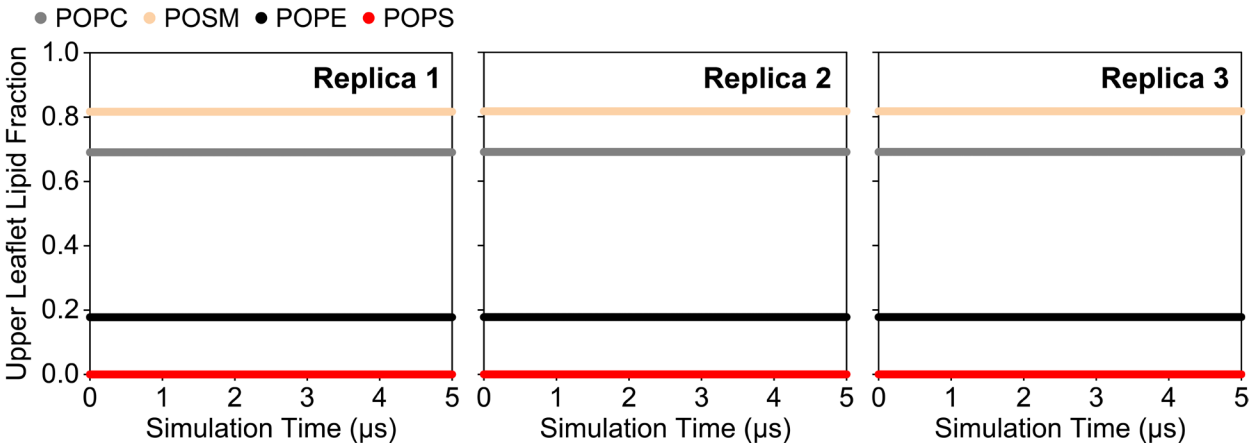

Figure S25: Upper leaflet lipid fraction as a function of simulation time for each lipid species (POPC, POSM, POPE, POPS) in RBC membranes simulated with P9 across three independent replicas. The 'Upper Leaflet Lipid Fraction' is defined as the number of a given lipid type in the upper leaflet divided by the total number of that lipid type across both leaflets. Flat profiles for all lipids across replicas indicate no flip-flop events for any lipid species.

Supplementary References

(1) Daina, A.; Michielin, O.; Zoete, V. SwissADME: a free web tool to evaluate pharmacokinetics, drug-likeness and medicinal chemistry friendliness of small molecules. *Scientific Reports* **2017**, *7* (1), 42717. DOI: 10.1038/srep42717.

(2) Pedersen, K. B.; Ingólfsson, H. I.; Ramirez-Echemendia, D. P.; Borges-Araújo, L.; Andreasen, M. D.; Empereur-mot, C.; Melcr, J.; Ozturk, T. N.; Bennett, W. F. D.; Kjølbye, L. R.; et al. The Martini 3 Lipidome: Expanded and Refined Parameters Improve Lipid Phase Behavior. *ACS Central Science* **2025**, *11* (9), 1598-1610. DOI: 10.1021/acscentsci.5c00755.

(3) Wu, E. L.; Cheng, X.; Jo, S.; Rui, H.; Song, K. C.; Dávila-Contreras, E. M.; Qi, Y.; Lee, J.; Monje-Galvan, V.; Venable, R. M.; et al. CHARMM-GUI Membrane Builder toward realistic biological membrane simulations. *Journal of Computational Chemistry* **2014**, *35* (27), 1997-2004. DOI: https://doi.org/10.1002/jcc.23702.

(4) Piggot, T. J.; Holdbrook, D. A.; Khalid, S. Electroporation of the E. coli and S. Aureus Membranes: Molecular Dynamics Simulations of Complex Bacterial Membranes. *The Journal of Physical Chemistry B* **2011**, *115* (45), 13381-13388. DOI: 10.1021/jp207013v.

(5) Witzke, S.; Petersen, M.; Carpenter, T. S.; Khalid, S. Molecular Dynamics Simulations Reveal the Conformational Flexibility of Lipid II and Its Loose Association with the Defensin Plectasin in the Staphylococcus aureus Membrane. *Biochemistry* **2016**, *55* (23), 3303-3314. DOI: 10.1021/acs.biochem.5b01315.

(6) Richardson, J. D.; Van Lehn, R. C. Elucidating the Impact of Red Blood Cell Membrane Components on Melittin-Induced Pore Formation with Molecular Dynamics Simulations. *The Journal of Physical Chemistry B* **2025**. DOI: 10.1021/acs.jpcb.5c04289.

(7) Zhao, W.; Róg, T.; Gurtovenko, A. A.; Vattulainen, I.; Karttunen, M. Atomic-Scale Structure and Electrostatics of Anionic Palmitoyloleoylphosphatidylglycerol Lipid Bilayers with Na+ Counterions. *Biophysical Journal* **2007**, *92* (4), 1114-1124. DOI: 10.1529/biophysj.106.086272.

(8) Wassenaar, T. A.; Ingólfsson, H. I.; Böckmann, R. A.; Tieleman, D. P.; Marrink, S. J. Computational Lipidomics with insane: A Versatile Tool for Generating Custom Membranes for Molecular Simulations. *Journal of Chemical Theory and Computation* **2015**, *11* (5), 2144-2155. DOI: 10.1021/acs.jctc.5b00209.

(9) Hanwell, M. D.; Curtis, D. E.; Lonie, D. C.; Vandermeersch, T.; Zurek, E.; Hutchison, G. R. Avogadro: an advanced semantic chemical editor, visualization, and analysis platform. *Journal of Cheminformatics* **2012**, *4* (1), 17. DOI: 10.1186/1758-2946-4-17.

(10) Vanommeslaeghe, K.; Hatcher, E.; Acharya, C.; Kundu, S.; Zhong, S.; Shim, J.; Darian, E.; Guvench, O.; Lopes, P.; Vorobyov, I.; et al. CHARMM general force field: A force field for drug-like molecules compatible with the CHARMM all-atom additive biological force fields. *Journal of Computational Chemistry* **2010**, *31* (4), 671-690. DOI: https://doi.org/10.1002/jcc.21367.

(11) Choi, Y. K.; Park, S.-J.; Park, S.; Kim, S.; Kern, N. R.; Lee, J.; Im, W. CHARMM-GUI Polymer Builder for Modeling and Simulation of Synthetic Polymers. *Journal of Chemical Theory and Computation* **2021**, *17* (4), 2431-2443. DOI: 10.1021/acs.jctc.1c00169.

(12) Tribello, G. A.; Bonomi, M.; Branduardi, D.; Camilloni, C.; Bussi, G. PLUMED 2: New feathers for an old bird. *Computer Physics Communications* **2014**, *185* (2), 604-613. DOI: https://doi.org/10.1016/j.cpc.2013.09.018.

(13) Mahajan, S.; Tang, T. Automated Parameterization of Coarse-Grained Polyethylenimine under a Martini Framework. *Journal of Chemical Information and Modeling* **2023**, *63* (14), 4328-4341. DOI: 10.1021/acs.jcim.3c00103.

(14) Mahajan, S.; Tang, T. Martini coarse-grained model for polyethylenimine. *Journal of Computational Chemistry* **2019**, *40* (3), 607-618. DOI: https://doi.org/10.1002/jcc.25747.

(15) Alessandri, R.; Barnoud, J.; Gertsen, A. S.; Patmanidis, I.; de Vries, A. H.; Souza, P. C. T.; Marrink, S. J. Martini 3 Coarse-Grained Force Field: Small Molecules. *Advanced Theory and Simulations* **2022**, *5* (1), 2100391. DOI: https://doi.org/10.1002/adts.202100391.

(16) Grossfield, A. *"WHAM: an implementation of the weighted histogram analysis method"*. http://membrane.urmc.rochester.edu/content/wham/.

(17) Souza, P. C. T.; Alessandri, R.; Barnoud, J.; Thallmair, S.; Faustino, I.; Grünewald, F.; Patmanidis, I.; Abdizadeh, H.; Bruininks, B. M. H.; Wassenaar, T. A.; et al. Martini 3: a general purpose force field for coarse-grained molecular dynamics. *Nature Methods* **2021**, *18* (4), 382-388. DOI: 10.1038/s41592-021-01098-3.

(18) Grünewald, F.; Alessandri, R.; Kroon, P. C.; Monticelli, L.; Souza, P. C. T.; Marrink, S. J. Polyply; a python suite for facilitating simulations of macromolecules and nanomaterials. *Nature Communications* **2022**, *13* (1), 68. DOI: 10.1038/s41467-021-27627-4.